SIAM J. SCI. COMPUT.
Vol. 47, No. 4, pp. B846–B874

RANDOM BATCH EWALD METHOD FOR DIELECTRICALLY CONFINED COULOMB SYSTEMS*

ZECHENG GAN†, XUANZHAO GAO‡, JIUYANG LIANG§, AND ZHENLI XU¶

Abstract. Quasi two-dimensional (quasi-2D) Coulomb systems have drawn widespread interest. The reduced symmetry of these systems leads to complex collective behaviors yet simultaneously poses significant challenges for particle-based simulations. In this paper, a novel method is presented for efficiently simulating a collection of N charges confined in doubly periodic slabs, with the extension to scenarios involving dielectric jumps at slab boundaries. Unlike existing methods, the method is insensitive to the aspect ratio of the simulation box, and it achieves optimal $\mathcal{O}(N)$ complexity and strong parallel scalability, thanks to the random batch Ewald (RBE) approach. Moreover, the additional cost for polarization contributions, represented as image reflection series, is reduced to a negligible cost via combining the RBE with an efficient structure factor coefficient recalibration technique in k-space. Explicit formulas for optimal parameter choices of the algorithm are provided through error estimates, together with a rigorous proof. Finally, we demonstrate the accuracy, efficiency, and scalability of our method, called RBE2D, via numerical tests across a variety of prototype systems. An excellent agreement between RBE2D and the particle-particle particle-mesh method (PPPM) is observed, with a significant reduction in the computational cost and improved strong scalability, demonstrating that it is a promising method for a broad range of charged systems under quasi-2D confinement.

Key words. molecular dynamics, quasi-2D Coulomb system, random batch Ewald, dielectric interfaces

MSC codes. 82M37, 65C35, 65T50, 65Y05

DOI. 10.1137/24M1655809

1. Introduction.

Quasi two-dimensional (quasi-2D) Coulomb systems [45], which are macroscopic in two dimensions but with atomic-size thickness other dimensions, have caught much attention in many areas of science and engineering. Due

*Submitted to the journal's Software, High-Performance Computing, and Computational Science and Engineering section April 22, 2024; accepted for publication (in revised form) March 13, 2025; published electronically July 14, 2025.

https://doi.org/10.1137/24M1655809

Funding: The work of first and second authors is supported by the Natural Science Foundation of China (grant 12201146); Natural Science Foundation of Guangdong (grant 2023A1515012197); Basic and applied basic research project of Guangzhou (grant 2023A04J0054); and Guangzhou-HKUST(GZ) joint research project (grants 2023A03J0003 and 2024A03J0606). The work of third and fourth authors is supported by the Natural Science Foundation of China (grants 12325113, 12426304, and 12401570) and the Science and Technology Commission of Shanghai Municipality (grant 23JC1402300). The work of third author is partially supported by the China Postdoctoral Science Foundation (grant 2024M751948). The authors also acknowledge support from the HPC center of Shanghai Jiao Tong University.

†Thrust of Advanced Materials and Guangzhou Municipal Key Laboratory of Materials Informatics, The Hong Kong University of Science and Technology (Guangzhou), Guangdong, China; and Department of Mathematics, The Hong Kong University of Science and Technology, Hong Kong SAR, China (zechenggan@ust.hk).

‡Thrust of Advanced Materials, The Hong Kong University of Science and Technology (Guangzhou), Guangdong, China; and Department of Physics, The Hong Kong University of Science and Technology, Hong Kong SAR, China (xz.gao@connect.ust.hk).

§School of Mathematical Sciences, Shanghai Jiao Tong University, Shanghai, 200240 China; and Center for Computational Mathematics, Flatiron Institute, Simons Foundation, New York, NY 10010 USA (liangjiuyang@sjtu.edu.cn, jliang@flatironinstitute.org).

¶School of Mathematical Sciences, MOE-LSC and CMA-Shanghai, Shanghai Jiao Tong University, Shanghai, 200240 People's Republic of China (xuzl@sjtu.edu.cn).

to the confinement effect, such systems can exhibit various interesting behaviors for future nanotechnologies; prototype examples include graphene [48], metal dichalcogenide monolayers [33], and colloidal monolayers [43]. Among quasi-2D systems, charged systems under dielectric slab confinement are of particular interest. The dielectric confinement is relevant to a wide range of systems and phenomena, including water/electrolytes/ionic liquids confined in thin films [52], ion transportation in nanopores [67], and self-assembly of colloidal/polymer monolayers [30]. For particle-based simulations of isotropic Coulomb systems, deterministic algorithms with complexity of $\mathcal{O}(N)$ or $\mathcal{O}(N \log N)$ have been developed, which usually fall into one of the two categories: fast multipole methods (FMMs) [20, 7, 65] and fast Fourier transform (FFT) based Ewald-splitting methods [22, 9, 15]. Noteworthy is that a new alternative, namely the random batch Ewald (RBE) method [29], has been proposed recently. RBE adopts an importance sampling strategy in $\boldsymbol{k}$-space and scales optimally as $\mathcal{O}(N)$ with reduced variances. RBE has been successfully applied to large-scale simulations of Coulomb systems under various ensembles [36, 37, 35] but so far is still limited to fully periodic cases. For confined quasi-2D Coulomb systems, the joint impact of the long-range Coulomb interaction, sharp dielectric interface conditions, and the reduced symmetry of quasi-2D geometry poses significant challenges for efficient and accurate particle-based simulations.

Over the past decades, numerous methods have been developed in the literature for quasi-2D Coulomb systems; most rely on modifications to the FMM and FFT-based Ewald methods. One important work is the Ewald2D method [50], which directly applies the Ewald-splitting technique for quasi-2D systems; it scales as $\mathcal{O}(N^2)$ and is found to be slowly convergent due to the oscillatory nature of the Green's function for quasi-2D geometry. To further accelerate the convergence of the quasi-2D lattice summation, more methods have been proposed, including the MMM2D method [4], the SOEwald2D method [19], the periodic FMM method [62], and the spectral Ewald method [41]. Instead of exactly solving the quasi-2D problem, alternative approaches are to approximate the quasi-2D summations by 3D periodic summations with correction terms, such as the Yeh–Berkowitz (YB) correction [63] and the electrostatic layer correction (ELC) [2]. These correction methods effectively reduce the computational cost and are simple to implement, but they lack control of accuracy.

The methods mentioned above encounter challenges when addressing sharp dielectric interfaces. In recent years, various strategies have been developed to effectively simulate dielectrically confined quasi-2D systems. These approaches address the polarization effect either by introducing image charges for slab interfaces, effectively transforming the system into a homogeneous one (albeit with a considerable increase in thickness along the z-direction) [59, 60, 13, 66, 39], or by numerically solving the Poisson equation with interface conditions [44, 47, 42]. We will not delve into a comprehensive review and comparison of these methods; instead, we will highlight two crucial aspects: (1) they all rely on either FMM or FFT to achieve $\mathcal{O}(N)$ or $\mathcal{O}(N \log N)$ complexity, respectively; and (2) the computational cost significantly increases compared to the homogeneous case, especially for *strongly confined* systems (i.e., with a large aspect ratio of simulation box). In this scenario, FFT-based methods require a significant increase in resolution to accommodate for the extended system thickness (i.e., zero-padding), while FMM-based methods require incorporating more near-field contributions and solving a possibly ill-conditioned linear system [51].

In this paper, we propose a novel method, namely the random batch Ewald2D method (RBE2D), for efficient and accurate simulations of quasi-2D charged systems

under dielectric confinement. We first present the reformulation for the quasi-2D Ewald sum into a Ewald3D sum with an ELC term and an infinite boundary correction (IBC) term. Rigorous error analysis is also presented, justifying the optimal parameter choices for a given accuracy. Then RBE is applied to achieve $\mathcal{O}(N)$ complexity: the stochastic approximation has reduced variances thanks to an importance sampling strategy and coupling with a proper thermostat in molecular dynamics (MD) simulations. For systems with dielectric mismatch, the subtle dielectric interface problem is reduced to a homogeneous problem via image charge reflection; we further recalibrate the structure factor coefficients for the image series in $\boldsymbol{k}$-space, enabling the computation of the polarization contributions with minimal overhead. The main advantage of our method compared with existing methods is twofold: (1) our method relies on a random batch sampling strategy in $\boldsymbol{k}$-space to achieve linear scaling, and thus it is highly efficient and has strong scalability; (2) our method is mesh-free and can be applied to strongly confined systems with negligible extra cost. Finally, numerical tests are presented across a variety of prototype systems, including symmetric/asymmetric electrolytes near neutral/nonneutral slabs in an implicit solvent, and all-atom simulations for confined water molecules, validating the accuracy, efficiency, and scalability of the RBE2D method.

The rest of the paper is organized as follows. In section 2, a comprehensive review of the Ewald2D summation is provided; then the RBE2D method is discussed in detail. In section 3, we introduce fast algorithms for treating the dielectric interfaces and extend the RBE2D method to systems under dielectric confinement. In sections 4 and 5, the accuracy, efficiency, and scalability of the RBE2D method are demonstrated via various numerical tests. Finally, the paper is concluded in section 6.

2. Random batch Ewald method for quasi-2D Coulomb systems. In this section, we first provide a comprehensive review of the commonly used summation formulas for quasi-2D Coulomb systems. Then we discuss the reformulation for the Ewald2D summation and the RBE2D method along with detailed error analysis.

2.1. Quasi-2D lattice summations. Quasi-2D systems are usually modeled as a rectangular domain Ω_{Q2D}, with doubly periodic boundary conditions in xy and free-space boundary condition in z. Side lengths of the simulation cell are L_x, L_y, and H in x, y, and z, respectively. The confined particles are modeled as point charges inside Ω_{Q2D}, with charge q_i and location $\boldsymbol{r}_i$, for $i \in \{1, \dots, N\}$. Also see Figure 1(a) for a 3D illustration. Typically, we assume $H < L_x = L_y$ due to confinement. We first focus on the homogeneous case in this section, and the extension to dielectric confinement case, as illustrated in Figure 1(b), will be discussed in section 3.

The total electrostatic energy U reads

$$U = \frac{1}{2} {\sum_{\boldsymbol{n}}}' \sum_{i,j=1}^{N} q_i q_j \frac{1}{|\boldsymbol{r}_{ij} + \boldsymbol{\ell}|}\,, \tag{2.1}$$

where $\boldsymbol{n} = \big(n_x, n_y\big)$ with $n_x,\, n_y \in \mathbb{Z}$, $\boldsymbol{r}_{ij} = \boldsymbol{r}_i - \boldsymbol{r}_j$, and $\boldsymbol{\ell} = \big(n_x L_x, n_y L_y, 0\big)$; i.e., we sum over periodic replicas in xy directions. It is understood that the singular term when $i = j$ and $\boldsymbol{n} = \boldsymbol{0}$ needs to be excluded, which is denoted as $\sum'$. Furthermore, the system must satisfy the total charge neutrality condition

$$\sum_{i=1}^{N} q_i = 0\,, \tag{2.2}$$

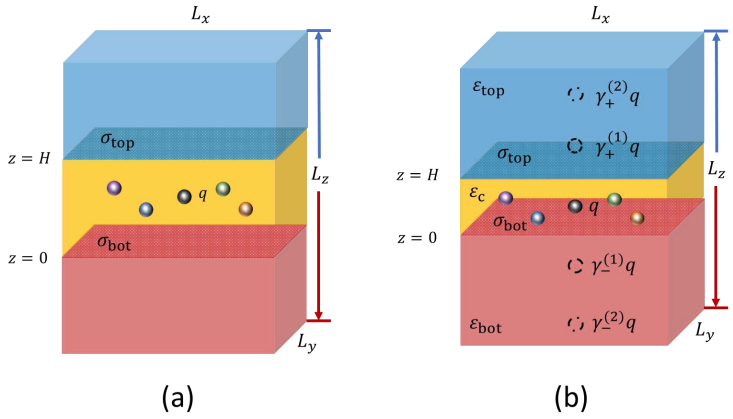

FIG. 1. *3D illustrations for* (a) *the quasi-2D system confined by two slabs without dielectric interfaces and* (b) *with two dielectric interfaces. The slabs are located at* $z = 0$ *and* $z = H$*. In* (b)*, the dashed circles indicate the image charges of* q *resulting from the reflection between the two interfaces. The magnitude of the* l*th layer of images is altered by factors of* $\gamma_{\pm}^{(l)}$*.*

so that the electrostatic energy and forces are well defined. Note that for 3D-periodic systems, the dipole moment must also be fixed to ensure that the sum is well defined [54, 2]. The difficulty of calculating (2.1) is twofold: (1) due to the long-range nature of the Coulomb potential, the lattice sum is slowly convergent, and one cannot just truncate the sum at a certain finite cutoff distance; (2) besides the long-range part, the Coulomb potential is also singular as $\boldsymbol{r} \to \mathbf{0}$, and as a result one cannot simply deal with it via Fourier transform due to the nonsmoothness.

To overcome these difficulties, one can use the so-called *Ewald-splitting* technique [16] to decompose the Coulomb kernels into the sum of two components as

$$\frac{1}{r} = \frac{\operatorname{erf}(\alpha r)}{r} + \frac{\operatorname{erfc}(\alpha r)}{r} \tag{2.3}$$

for any constant $\alpha > 0$, where the error function $\operatorname{erf}(\cdot)$ is defined as

$$\operatorname{erf}(x) := \frac{2}{\sqrt{\pi}} \int_0^x e^{-u^2} du\,, \tag{2.4}$$

and the error complementary function is $\operatorname{erfc}(x) := 1 - \operatorname{erf}(x)$. After splitting, the singular and long-range Coulomb kernel is separated into a singular short-range kernel and a smooth long-range kernel, which can be efficiently handled in real and reciprocal spaces, respectively. It has been shown that under the charge neutrality condition (2.2), the quasi-2D lattice sum U given by (2.1) can be written as [50, 57]

$$U = U_{\text{real}} + U_{\text{Fourier}}, \tag{2.5}$$

where

$$U_{\text{real}} = \frac{1}{2} {\sum_{\boldsymbol{n}}}' \sum_{i,j=1}^{N} q_i q_j \frac{\operatorname{erfc}(\alpha\,|\boldsymbol{r}_{ij} + \boldsymbol{\ell}|)}{|\boldsymbol{r}_{ij} + \boldsymbol{\ell}|}\,, \tag{2.6}$$

$$U_{\text{Fourier}} = \frac{\pi}{2L_x L_y} \sum_{i,j=1}^{N} q_i q_j {\sum_{\boldsymbol{h}}}' \frac{e^{\iota \boldsymbol{h}\cdot\boldsymbol{r}_{ij}}}{h} \mathcal{G}_\alpha(h, z_{ij}) - \frac{\alpha}{\sqrt{\pi}} \sum_{i=1}^{N} q_i^2 + \mathcal{J}_0\,. \tag{2.7}$$

Here the reciprocal lattice vector is defined as $\boldsymbol{h} = 2\pi\left(n_x/L_x, n_y/L_y, 0\right)$, $\iota = \sqrt{-1}$, $z_{ij} = z_i - z_j$, and

$$\mathcal{G}_\alpha(h, z_{ij}) := \left[e^{hz_{ij}}\mathrm{erfc}\left(\frac{h}{2\alpha} + \alpha z_{ij}\right) + e^{-hz_{ij}}\mathrm{erfc}\left(\frac{h}{2\alpha} - \alpha z_{ij}\right)\right] \tag{2.8}$$

with $h = |\boldsymbol{h}|$. The **0**th mode correction $\mathcal{J}_0$ reads

$$\mathcal{J}_0 = \frac{-\pi}{L_x L_y}\sum_{i,j=1}^{N} q_i q_j \left[z_{ij}\mathrm{erf}\left(\alpha z_{ij}\right) + \frac{1}{\alpha\sqrt{\pi}}e^{-\alpha^2 z_{ij}^2}\right]. \tag{2.9}$$

Equations (2.6)–(2.9) are the well-known exact Ewald2D summation formulas [50, 24]. In contrast to the 3D-periodic case where the Ewald sum is conditionally convergent, the Ewald2D sum is absolutely convergent. Note that the optimal complexity of the 3D-periodic Ewald sum is $\mathcal{O}(N^{3/2})$ when α and the truncation strategies for real and Fourier space calculations are chosen appropriately [18, 31]. In comparison, the computational cost for (2.6)–(2.9) is more expensive due to the complicated summation form in Fourier space. By properly choosing an optimal α, it takes the best-known $\mathcal{O}(N^2)$ complexity [41, 21, 45], which is worse than Ewald3D summations, and limits its application to large-scale simulations.

2.2. Reformulation for Ewald2D summation. In this section, we present a reformulation for the Ewald2D sum, which reduces the Ewald2D sum (2.6)–(2.9) to a simpler Ewald3D sum complemented by an infinite boundary correction (IBC) and electrostatic layer corrections (ELCs) [49] based on which efficient algorithms can be further developed.

We first use the following identity [14]:

$$I(\omega,\nu) = \frac{\pi}{2\omega}\left[e^{\omega\nu}\mathrm{erfc}\left(\omega + \frac{\nu}{2}\right) + e^{-\omega\nu}\mathrm{erfc}\left(\omega - \frac{\nu}{2}\right)\right] = e^{-\omega^2}\int_{-\infty}^{\infty}\frac{e^{-t^2}}{\omega^2 + t^2}e^{\iota t\nu}dt\,. \tag{2.10}$$

Taking the limit $\omega \to 0$ and isolating the divergence, one has the following identity:

$$I_0(\nu) = -\pi\left[\nu\mathrm{erf}\left(\frac{\nu}{2}\right) + \frac{2e^{-\frac{\nu^2}{4}}}{\sqrt{\pi}}\right] = \int_{-\infty}^{\infty}\frac{e^{-t^2}e^{\iota t\nu} - 1}{t^2}dt\,. \tag{2.11}$$

Applying (2.10) and (2.11) to (2.7) and (2.9) by taking $\omega = h/2\alpha$ and $\nu = 2\alpha z_{ij}$, one obtains the alternative expressions in integral forms:

$$U_{\mathrm{Fourier}} = \frac{1}{2\alpha L_x L_y}\sum_{i,j=1}^{N} q_i q_j {\sum_{\boldsymbol{h}}}' e^{\iota\boldsymbol{h}\cdot\boldsymbol{r}_{ij}}\int_{-\infty}^{\infty}\frac{e^{-\frac{h^2}{4\alpha^2} - t^2}}{\frac{h^2}{4\alpha^2} + t^2}e^{2\iota\alpha z_{ij}t}dt - \frac{\alpha}{\sqrt{\pi}}\sum_{i=1}^{N} q_i^2 + \mathcal{J}_0, \tag{2.12}$$

with

$$\mathcal{J}_0 = \frac{1}{2\alpha L_x L_y}\sum_{i,j=1}^{N} q_i q_j \int_{-\infty}^{\infty}\frac{e^{-t^2}e^{2\iota\alpha z_{ij}t} - 1}{t^2}dt. \tag{2.13}$$

Due to the smoothness and exponential decay of the integrands, discretizing the integrals via the trapezoidal rule yields spectral convergence [58]. The resulting discretized formulation and error estimates are summarized in Theorem 2.1.

THEOREM 2.1 (Ewald2D reformulation and its error estimate). *Assume $L_z \geq H$; discretizing the integrals in* (2.12) *via the trapezoidal rule with mesh size $\pi/\alpha L_z$, one will have*

(2.14)
$$U_{\text{Fourier}} = \frac{2\pi}{L_x L_y L_z} {\sum_{\boldsymbol{k}}}' \frac{e^{-\frac{k^2}{4\alpha^2}}}{k^2} \left| \sum_{i=1}^{N} q_i e^{\iota \boldsymbol{k}\cdot \boldsymbol{r}_i} \right|^2 - \frac{\alpha}{\sqrt{\pi}} \sum_{i=1}^{N} q_i^2 + U_{\text{IBC}} + U_{\text{ELC}} + U_{\text{err}} ,$$

where $\boldsymbol{k} = 2\pi(n_x/L_x, n_y/L_y, n_z/L_z)$ with $n_x, n_y, n_z \in \mathbb{Z}$, the first two terms on the right-hand side (RHS) are in the form of Ewald3D summation; and

(2.15)
$$U_{\text{IBC}} := \frac{2\pi}{L_x L_y L_z} \left(\sum_{i=1}^{N} q_i z_i \right)^2, \qquad U_{\text{ELC}} := \frac{2\pi}{L_x L_y} \sum_{i,j} q_i q_j {\sum_{\boldsymbol{h}}}' \left[\frac{e^{\iota \boldsymbol{h}\cdot \boldsymbol{r}_{ij}}}{h} \frac{\cosh(h z_{ij})}{1 - e^{h L_z}} \right]$$

are the IBC [63] *and ELC* [2] *terms found earlier separately, and U_{err} is the remainder error term due to trapezoidal discretization. The last two terms decay as*

$$|U_{\text{ELC}}| \sim \mathcal{O}\left(e^{-\frac{2\pi(L_z - H)}{\max\{L_x, L_y\}}} \right) \quad \textit{and} \quad |U_{\text{err}}| \sim \mathcal{O}\left(e^{-\alpha^2 (L_z - H)^2} \right), \tag{2.16}$$

respectively.

Proof. Through the error analysis of the trapezoidal rule provided in Appendix A, one has

(2.17)
$$\begin{aligned} &{\sum_{\boldsymbol{h}}}' e^{\iota \boldsymbol{h}\cdot \boldsymbol{r}_{ij}} \int_{-\infty}^{\infty} \frac{e^{-\frac{h^2}{4\alpha^2} - t^2}}{\frac{h^2}{4\alpha^2} + t^2} e^{2\iota\alpha z_{ij} t} dt + \int_{-\infty}^{\infty} \frac{e^{-t^2} e^{2\iota\alpha z_{ij} t} - 1}{t^2} dt \\ &= \frac{\pi}{\alpha L_z} {\sum_{\boldsymbol{k}}}' \frac{e^{-\frac{k^2}{4\alpha^2}}}{k^2} e^{\iota \boldsymbol{k}\cdot \boldsymbol{r}_{ij}} + \frac{4\alpha\pi}{L_z} \lim_{k_z \to 0} \frac{e^{-\frac{k_z^2}{4\alpha^2}} e^{\iota k_z z_{ij}} - 1}{k_z^2} + 4\alpha\pi {\sum_{h}}' \frac{e^{\iota \boldsymbol{h}\cdot \boldsymbol{r}_{ij}}}{h} \frac{\cosh(h z_{ij})}{1 - e^{h L_z}} \\ &\quad + \mathcal{O}\left(e^{-\alpha^2 (L_z - |z_{ij}|)^2} \right). \end{aligned}$$

By substituting (2.17) into (2.12), it is observed that the first two terms on the RHS of (2.17) correspond to the first term and the IBC term in (2.14), respectively. The third term in (2.17) acts as the ELC term in (2.14). ∎

Clearly, the first two terms in (2.14) closely resemble the Fourier component of the Ewald3D summation [16, 24]. It can be understood as constructing a fully periodic system, referred to as Ω_{3D}, which shares the same particle configuration and xy dimensions as the original quasi-2D system Ω_{Q2D}, but extending the dimension in z from H to L_z (see Figure 1(a)). This extra layer with thickness of $L_z - H$ (containing no particles) is usually called a "vacuum layer." Now according to Theorem 2.1, one has

$$U_{\text{Fourier}}(\Omega_{\text{Q2D}}) = U_{\text{Fourier}}(\Omega_{\text{3D}}) + U_{\text{IBC}} + U_{\text{ELC}} + U_{\text{err}}. \tag{2.18}$$

The IBC and ELC terms can be understood to correct the unwanted z-replicas effect and boundary conditions at infinity when approximating the quasi-2D system as a fully periodic one with vacuum layers [2, 63].

The U_{ELC} and U_{err} terms are usually disregarded by mainstream MD software [56, 1], and the remaining terms, $U_{\text{Fourier}}(\Omega_{\text{3D}})$ and U_{IBC}, can be conveniently evaluated via FFT-based Ewald3D methods. However, (2.16) indicates that to guarantee both the ELC and U_{err} terms contribute below a certain tolerance ε, the choice for the thickness L_z should satisfy

$$L_z \geq H + \max\left\{ \frac{\max\{L_x, L_y\}}{2\pi} \log\frac{1}{\varepsilon},\ \frac{1}{\alpha}\sqrt{\log\frac{1}{\varepsilon}} \right\}, \tag{2.19}$$

which means one may need to choose a vacuum layer thickness much larger than H if $\alpha \ll 1/H$ or $\max\{L_x, L_y\} \gg H$. For FFT-based methods, this means one will need to discretize the whole extended domain with vacuum layers, which will greatly increase the computational cost.

Remark 2.2. It is interesting to observe that the thickness of the vacuum layer $(L_z - H)$ is determined by the system dimensions in xy and the Ewald splitting parameter α, but is independent of H.

2.3. Random batch Ewald2D method. We now introduce the random batch Ewald2D (RBE2D) method. Instead of deterministically computing the $\boldsymbol{k}$-space sum given by (2.14) either directly or via FFT, we now evaluate it through a stochastic approximation, namely, the random "mini-batch" sampling [26]. Notice that the low $\boldsymbol{k}$ modes are more important due to the $e^{-k^2/(4\alpha^2)}$ factor; an importance sampling strategy was further developed for variance reduction. The random batch Ewald (RBE) method has recently been developed for fully periodic systems [29, 36, 38], and here we extend it to quasi-2D systems.

The long-range component of the electrostatic force exerted on the ith particle is given by $\boldsymbol{F}_i^{\text{Fourier}} = -\nabla_{\boldsymbol{r}_i} U_{\text{Fourier}}$, and its random batch approximation is denoted as

$$\tilde{\boldsymbol{F}}_i^{\text{Fourier}} = -\sum_{\ell=1}^{P} \frac{S}{P} \frac{4\pi q_i \boldsymbol{k}_\ell}{V k_\ell^2} \text{Im}\left(e^{-\iota \boldsymbol{k}_\ell \cdot \boldsymbol{r}_i} \rho(\boldsymbol{k}_\ell) \right), \tag{2.20}$$

where P is the batch size, $V = L_x L_y L_z$ is the volume of the extended simulation domain Ω_{3D}, $\rho(\boldsymbol{k})$ is the *structure factor* defined as

$$\rho(\boldsymbol{k}) = \sum_{j=1}^{N} q_j e^{\iota \boldsymbol{k} \cdot \boldsymbol{r}_j}, \tag{2.21}$$

and S is the normalizing constant,

$$S = \sum_{\boldsymbol{k} \neq 0} e^{-k^2/(4\alpha^2)}. \tag{2.22}$$

In MD simulations, it is convenient to employ the Metropolis algorithm [46] to sample from $\mathscr{P}(\boldsymbol{k}) = e^{-k^2/(4\alpha^2)}/S$. Our numerical experiments indicate that the average acceptance rate exceeds 90%, rendering the correlation between samples negligible. In practice, one can further introduce a downsampling factor $\mathcal{P}$, namely, select 1 sample from every $\mathcal{P}$ sampling steps to further eliminate the correlation (we take $\mathcal{P} = 5$ in our calculations, and the autocorrelation decays to approximately 10^{-3}, which is already a very small value), and this downsampling factor does not compromise overall efficiency, as the cost of the sampling procedure is relatively low. Note that

alternative methods, such as directly sampling from discrete multivariate Gaussian distributions by truncating at certain $k_{\max}$, are also applicable.

For quasi-2D systems, the RBE2D method offers a particular advantage: it is mesh-free, so that, unlike existing grid-based fast algorithms, the computational cost is independent of the added vacuum layer thickness. This statement is justified more rigorously in Theorem 2.3. In the theorem, one utilizes the Debye–Hückel (DH) assumption for nonideal electrolytes [34] (also see Appendix F in [19]), where the ensemble-averaged charge distributions around a charged particle follow the Boltzmann distribution.

THEOREM 2.3. *Denote the fluctuation of the random batch approximation in force by* $\boldsymbol{\Xi}_{\boldsymbol{F},i} = \tilde{\boldsymbol{F}}_i^{\text{Fourier}} - \boldsymbol{F}_i^{\text{Fourier}}$. *The random variable* $\boldsymbol{\Xi}_{\boldsymbol{F},i}$ *has zero expectation, i.e.,* $\mathbb{E}\boldsymbol{\Xi}_{\boldsymbol{F},i} = \mathbf{0}$, *and its variance is given by*

$$\mathbb{E}|\boldsymbol{\Xi}_{\boldsymbol{F},i}|^2 = \frac{1}{P}\left[\frac{(4\pi q_i)^2 S}{V^2}\sum_{\boldsymbol{k}\neq\mathbf{0}}\frac{e^{-k^2/(4\alpha^2)}}{k^2}\left|\mathrm{Im}\left(e^{-\iota\boldsymbol{k}_\ell\cdot\boldsymbol{r}_i}\rho(\boldsymbol{k}_\ell)\right)\right|^2 - |\boldsymbol{F}_i^{\text{Fourier}}|^2\right], \tag{2.23}$$

which is bounded and scales as $\mathcal{O}(1/P)$. *Furthermore, under the DH assumption,* $\mathbb{E}|\boldsymbol{\Xi}_{\boldsymbol{F},i}|^2$ *is independent of both the particle number* N *and the size* L_z.

Proof. The property of unbiasedness in Theorem 2.3 is straightforward and guarantees the consistency of the stochastic approximation, i.e., $\mathbb{E}\tilde{\boldsymbol{F}}_i^{\text{Fourier}} = \mathbb{E}\boldsymbol{F}_i^{\text{Fourier}}$. Let us now consider the variance. By the DH assumption, the structure factor term in (2.23) is bounded by a constant C [29] for $\boldsymbol{k}\neq\mathbf{0}$,

$$\left|\mathrm{Im}\left(e^{-\iota\boldsymbol{k}\cdot\boldsymbol{r}_i}\rho(\boldsymbol{k})\right)\right|^2 \leq C, \tag{2.24}$$

and vanishes for $\boldsymbol{k}=\mathbf{0}$. Further by the monotonicity of the Gaussian on $[0,+\infty)$, it follows that

$$\mathbb{E}|\boldsymbol{\Xi}_{\boldsymbol{F},i}|^2 \leq \frac{8CSq_i^2}{PV}\int_0^\infty e^{-k^2/(4\alpha^2)}dk = \frac{8\sqrt{\pi}\alpha CSq_i^2}{PV}. \tag{2.25}$$

Analogously, one can obtain the following estimate for the normalization constant S:

$$S \leq \frac{V}{(2\pi)^3}\int_0^\infty 4\pi k^2 e^{-k^2/(4\alpha^2)}dk = \frac{\alpha^3 V}{\pi^{3/2}}. \tag{2.26}$$

Substituting (2.26) into (2.25) yields

$$\mathbb{E}|\boldsymbol{\Xi}_{\boldsymbol{F},i}|^2 \leq \frac{8\alpha^4 Cq_i^2}{\pi P} \sim \mathcal{O}\left(\frac{1}{P}\right), \tag{2.27}$$

which is independent of either N or L_z. ∎

Theorem 2.3 suggests that the variance in the random batch approximation can be effectively controlled by appropriately choosing the batch size P, which is independent of the particle number N. In the context of Ewald summation, typical choices for α are $(\sqrt{N}/V)^{1/3}$ for direct truncation [31] and $(N/V)^{1/3}$ for FFT-based calculation [10]. Now for the RBE2D method, it is clear that changing the vacuum layer thickness does not affect its efficiency. In practice, we set $\alpha \sim N^{1/3}/(L_xL_yH)^{1/3}$ (independent of L_z); then it is expected that the variance of the force remains at the same level as one changes L_z. This is further validated by numerical results in section 4.1.

2.4. Convergence and complexity of the RBE2D. In this section, we further examine the convergence and complexity of RBE2D accelerated MD simulations. First, we revisit the common purpose of MD simulations, which is to explore the configuration space and obtain static/dynamic ensemble-averaged properties by solving the equations of motion for N interacting particles. For example, consider the widely used canonical ensemble, where the system has fixed particle number N, volume V, and temperature T, which can be simulated as solving the following equations, namely, MD with Langevin thermostat [18]:

$$\begin{aligned} d\boldsymbol{r}_i &= \boldsymbol{v}_i dt, \\ m_i d\boldsymbol{v}_i &= [\boldsymbol{F}_i - \gamma \boldsymbol{v}_i]\, dt + \sqrt{2\gamma k_{\mathrm{B}} T} d\boldsymbol{W}_i, \end{aligned} \tag{2.28}$$

where $\boldsymbol{r}_i$, m_i, and $\boldsymbol{v}_i$ represent the position, mass, and velocity of the ith particle, respectively. $\boldsymbol{F}_i$ is the force exerted on the ith particle, $\{\boldsymbol{W}_i\}$ are independent and identically distributed (i.i.d.) Wiener processes, and γ is the reciprocal characteristic time scale associated with the thermostat. In practice, the stochastic differential equations are discretized with proper numerical schemes and integrated with time step Δt. Let $(\boldsymbol{r}_i, \boldsymbol{v}_i)$ be the solution to (2.28) with $\boldsymbol{F}_i = \boldsymbol{F}_i^{\mathrm{exact}}$, where $\boldsymbol{F}_i^{\mathrm{exact}}$ is the exact force on the ith particle; and let $(\widetilde{\boldsymbol{r}}_i, \widetilde{\boldsymbol{v}}_i)$ be the solution to the same set of equations but with RBE2D approximated force given by $\boldsymbol{F}_i = \boldsymbol{F}_i^{\mathrm{exact}} + \boldsymbol{\Xi}_{\boldsymbol{F},i}$. Then the relation between the two sets of solutions satisfies the following Theorem 2.4 [27].

THEOREM 2.4. *If the forces $\boldsymbol{F}_i$ are bounded and Lipschitz, and the fluctuation of stochastic force satisfies $\mathbb{E}\boldsymbol{\Xi}_{\boldsymbol{F},i} = 0$, then for any $t_{\mathrm{MD}} > 0$, there exists $C(t_{\mathrm{MD}}) > 0$ such that*

$$\sup_{t\in[0,t_{\mathrm{MD}}]} \sqrt{\frac{1}{N}\sum_{i=1}^{N} \mathbb{E}\left(|\boldsymbol{r}_i - \widetilde{\boldsymbol{r}}_i|^2 + |\boldsymbol{v}_i - \widetilde{\boldsymbol{v}}_i|^2\right)} \le C(t_{\mathrm{MD}})\sqrt{\Lambda \Delta t}. \tag{2.29}$$

Here, Λ is an upper bound for $\mathbb{E}|\boldsymbol{\Xi}_{\boldsymbol{F},i}|^2$, and one has $\Lambda \sim \mathcal{O}(1/P)$ due to Theorem 2.3.

Theorem 2.4 indicates that the RBE2D approximated dynamics is capable of capturing finite time structure and dynamic properties. For long-time simulations, additional assumptions are needed regarding force regularity [28]. It is worth noting that, although the Coulomb potential is neither bounded nor Lipschitz at $r = 0$, actual MD simulations will include the Lennard-Jones (LJ) potential, which provides a strong repulsive force at short inter-particle distance and prevents the particles from getting too close. As a result, the singularities in both the Coulomb and LJ potentials will not be reached in practice as long as the time step is properly chosen, allowing us to satisfy the condition of Theorem 2.4 for MD simulations.

Additionally, following Theorem 2.4, the fluctuations introduced by random batch approximation, $\boldsymbol{\Xi}_{\boldsymbol{F},i}$, can be physically understood as heating effects, which will cause a temperature drift for the system and is unwanted. For NVT (canonical) and NPT (isothermal–isobaric) ensembles, the heating effect can be eliminated by introducing appropriate thermostats such as the Langevin thermostat [17], the Nosé–Hoover (NH) thermostat [23], etc. With an additional weak-coupled bath on the Newtonian dynamics to avoid energy drift, the NVE (microcanonical) ensemble can also be accurately simulated with random batch-type approximations [37].

Next, we analyze the computational complexity of the RBE2D accelerated MD simulations. The detailed algorithm is summarized in Algorithm 2.1. In the RBE2D, the random batch importance sampling in (2.20) approximates the Fourier space force

Algorithm 2.1 (RBE2D accelerated molecular dynamics for quasi-2D systems).

1: Choose α, r_c (the cutoff in real space), Δt, the vacuum layer parameter L_z, and batch size P. Initialize the positions and velocities of ions as well as surface charge densities. Set N_T as the total MD time steps.
2: **for** n in $1 : N_T$ **do**
3: Sample P nonzero frequencies $\boldsymbol{k} \sim e^{-k^2/(4\alpha)}$ by the Metropolis procedure to form set $\mathcal{K}$.
4: The $\boldsymbol{k}$-space component of the force, $\boldsymbol{F}_i^{\text{Fourier}}$, is computed using the random batch approximation $\widetilde{\boldsymbol{F}}_i^{\text{Fourier}}$ with the P frequencies from the set $\mathcal{K}$.
5: The real space component of the force, $\boldsymbol{F}_i^{\text{real}}$, is computed by the neighbor list method.
6: Integrate the equations of motion for time step Δt with an appropriate thermostat and its corresponding integration scheme.
7: **end for**

by summing over P Fourier modes. At each step, P structure factors, $\{\rho(\boldsymbol{k}_\ell)\}_{\ell=1}^P$, are computed for all particles, resulting in a Fourier part complexity of $\mathcal{O}(PN)$. Furthermore, as shown in Theorems 2.3 and 2.4 and the analysis at the end of section 2.3, the RBE2D error does not grow as N or L_z increases when the batch size $P = \mathcal{O}(1)$ and $\alpha \sim N^{1/3}/(L_x L_y H)^{1/3}$ are provided. The real space part of the RBE2D is short-ranged due to the rapid decay of factor $\operatorname{erfc}(\alpha r)$ and can be directly truncated by introducing a cutoff r_c. As a result, the real space complexity is proportional to the product of N and the average number of neighbors within a volume of $4\pi r_c^3$ per particle. For a given truncation error tolerance, $r_c \sim \alpha^{-1}$, yielding a real space complexity $\sim \alpha^{-3} N/(L_x L_y H) = \mathcal{O}(1)$ per particle. As such, the total computational complexity is of $\mathcal{O}(N)$.

Besides its linear complexity, the RBE2D method offers two other significant advantages:

- Communication efficiency: The RBE2D method is embarrassingly parallel, requiring only a single global reduction of the structure factors for all $\mathcal{O}(P)$ samples when calculating the force using (2.20). This streamlined communication facilitates high scalability.
- Vacuum layer flexibility: The RBE2D is mesh-free, and choosing a larger vacuum layer thickness incurs no extra cost. This provides flexibility for one to always choose a proper L_z to guarantee accuracy, without sacrificing efficiency.

3. Quasi-2D systems under dielectric confinement. In this section, we extend the RBE2D to the challenging case of systems with dielectric jumps at the slab interfaces ($z = 0$ and $z = H$). We will first introduce the three-layer sandwich model and its computation by truncated image reflection series. Detailed analysis of the truncation error is presented, along with a recalibrated efficient formula for the computation of electrostatic energy and force with minimum extra cost. Finally, we summarize the algorithm framework to extend the RBE2D method to systems under dielectric confinement.

3.1. The three-layer sandwich model. A schematic of the three-layer sandwich model illustrating the dielectrically confined quasi-2D system is shown in

Figure 1(b). Two dielectric interfaces are introduced at $z = 0$ and $z = H$, dividing the system into three layers. These layers, from top to bottom, are labeled as Ω_{top}, Ω_{c}, and Ω_{bot}, with respective permittivities ε_{top}, ε_{c}, and ε_{bot}. Additionally, we still assume the total charge neutrality condition (2.2) is valid.

First, let us define the dimensionless dielectric contrasts at the interfaces as

$$\gamma_{\text{top}} = \frac{\varepsilon_{\text{c}} - \varepsilon_{\text{top}}}{\varepsilon_{\text{c}} + \varepsilon_{\text{top}}} \quad \text{and} \quad \gamma_{\text{bot}} = \frac{\varepsilon_{\text{c}} - \varepsilon_{\text{bot}}}{\varepsilon_{\text{c}} + \varepsilon_{\text{bot}}}. \tag{3.1}$$

Note that $|\gamma_{\text{top}}| \le 1$ and $|\gamma_{\text{bot}}| \le 1$ since $\varepsilon_{\text{c}}, \varepsilon_{\text{top}}, \varepsilon_{\text{bot}}$ are all positive. We are particularly interested in the electrostatic energy U^{c} for charges confined within the central layer $[0, H]$. The polarization contribution can be conveniently expressed as a series of image charges resulting from (1) periodic replications along xy by double periodicity and (2) mirror reflections along z (refer to [25] and also Figure 1(b)):

$$U^{\text{c}} = \frac{1}{2} \sum_{i,j=1}^{N} q_i q_j \left[{\sum_{\boldsymbol{n}}}' \frac{1}{|\boldsymbol{r}_{ij} + \boldsymbol{\ell}|} + \sum_{\boldsymbol{n}} \sum_{l=1}^{\infty} \left(\frac{\gamma_+^{(l)}}{\left|\boldsymbol{r}_i - \boldsymbol{r}_{j+}^{(l)} + \boldsymbol{\ell}\right|} + \frac{\gamma_-^{(l)}}{\left|\boldsymbol{r}_i - \boldsymbol{r}_{j-}^{(l)} + \boldsymbol{\ell}\right|} \right) \right], \tag{3.2}$$

where the factors for the lth-order image charges are $\gamma_+^{(l)} = \gamma_{\text{top}}^{\lfloor l/2 \rfloor} \gamma_{\text{bot}}^{\lceil l/2 \rceil}$ and $\gamma_-^{(l)} = \gamma_{\text{top}}^{\lceil l/2 \rceil} \gamma_{\text{bot}}^{\lfloor l/2 \rfloor}$. Here $+(-)$ corresponds to the image charges in Ω_{top} (Ω_{bot}). The notation $\lceil x \rceil$ ($\lfloor x \rfloor$) represents the "ceil" ("floor") function, and the positions of the lth-order image of charge q_j are given by $\boldsymbol{r}_{j\pm}^{(l)} = (x_j, y_j, z_{j\pm}^{(l)})$ with

$$z_{j+}^{(l)} = (-1)^l z_j + 2\lceil l/2 \rceil H \quad \text{and} \quad z_{j-}^{(l)} = (-1)^l z_j - 2\lfloor l/2 \rfloor H. \tag{3.3}$$

Clearly, compared to the previous homogeneous case, the extra polarization contribution in terms of image charge series can significantly impact the efficiency. This effect becomes more pronounced when $|\gamma_{\text{top}}\gamma_{\text{bot}}| \to 1$, as the convergence of the image series in (3.2) can become extremely slow.

To make the problem computationally feasible, existing methods [13, 12, 66] typically involve truncating the number of image charges in z at a certain reflection level $l = M$ and then correspondingly adjust the vacuum layer thickness by choosing $\hat{L}_M = (2M + 1)H$ so as to enclose all the M-level reflected images. Subsequently, an additional vacuum layer as a safe zone is introduced, increasing the system size in z to $L_z = \eta_z \hat{L}_M$ with $\eta_z > 1$. Unfortunately, so far there is no clear theoretical guidance about how to select parameters M and η_z, with some given accuracy requirement. Even so, due to the simplicity of image charge representation, this approach has still been widely adopted in practical simulations to account for the dielectric confinement effect.

In subsequent sections, we will investigate the choice of M and L_z based on the Ewald2D reformulation introduced in section 2.2. To the best of our knowledge, this work provides the first theoretical study on how M and L_z influence the error. It is worth noting that, regarding the parameter choice, conflicting conclusions were made in literature based on numerical tests. For example, when $|\gamma_{\text{top}}\gamma_{\text{bot}}| \approx 1$, dos Santos and Levin [13] found that approximately $M = 50$ levels of images are required to achieve satisfactory accuracy, while Yuan, Antila, and Luijten [66] suggest that choosing $M = 5$ is sufficient. In [66], it was also observed that choosing a very large M may lead to counterintuitive accuracy loss. Interestingly, our theoretical analysis below can provide explanations for all the subtle phenomena above.

3.2. Truncation error analysis for the image reflection series. To analyze the truncation error for the image series in (3.2) at a certain reflection level $l = M$, it is useful to first introduce the quasi-2D Poisson summation formula, summarized in Lemma 3.1.

LEMMA 3.1. *Let $f(\boldsymbol{\rho}, z)$ be a function which is doubly periodic in $\boldsymbol{\rho} = (x, y)$. Suppose that f has the Fourier transform $\tilde{f}$ and $\boldsymbol{r} = (\boldsymbol{\rho}, z)$; then one has*

$$\sum_{\boldsymbol{n}} f(\boldsymbol{r} + \boldsymbol{\ell}) = \frac{1}{2\pi L_x L_y} \sum_{\boldsymbol{k_\rho}} \int_{\mathbb{R}} \tilde{f}(\boldsymbol{k_\rho}, k_z) e^{\iota \boldsymbol{k_\rho} \cdot \boldsymbol{\rho}} e^{\iota k_z z} dk_z, \tag{3.4}$$

where $\boldsymbol{k_\rho} = 2\pi(n_x/L_x, n_y/L_y)$, and $\boldsymbol{\ell} = (n_x L_x, n_y L_y, 0)$.

Applying Lemma 3.1 to (3.2), one has

$$U^{\mathrm{c}} = \frac{1}{2} \sum_{i,j=1}^{N} q_i q_j {\sum_{\boldsymbol{n}}}' \frac{1}{|\boldsymbol{r}_{ij} + \boldsymbol{\ell}|} + \frac{\pi}{L_x L_y} \sum_{i,j=1}^{N} q_i q_j {\sum_{\boldsymbol{h}}}' \frac{e^{-\iota \boldsymbol{h} \cdot \boldsymbol{r}_{ij}}}{h} \beta_{ij}(h)\,, \tag{3.5}$$

where we recall $\boldsymbol{h} = 2\pi(n_x/L_x, n_y/L_y, 0)$. We leave the first term the same as in (2.1), which is the energy for a homogeneous quasi-2D Coulomb system, and

$$\beta_{ij}(h) := \sum_{l=1}^{\infty} \left[\gamma_+^{(l)} e^{-h\left|z_i - z_{j+}^{(l)}\right|} + \gamma_-^{(l)} e^{-h\left|z_i - z_{j-}^{(l)}\right|} \right]. \tag{3.6}$$

Substituting the definitions of $\gamma_\pm^{(l)}$ and (3.3) into (3.6) and rearranging terms, we obtain

$$\begin{aligned} \beta_{ij}(h) = \Big[& \gamma_{\mathrm{bot}} e^{-h|z_i + z_j|} + \gamma_{\mathrm{top}} e^{-h|2H - (z_i + z_j)|} \\ & + \gamma_{\mathrm{top}} \gamma_{\mathrm{bot}} \left(e^{-h|2H - z_{ij}|} + e^{-h|2H + z_{ij}|} \right) \Big] \zeta(h)\,, \end{aligned} \tag{3.7}$$

where

$$\zeta(h) := \sum_{n=0}^{\infty} \left(\gamma_{\mathrm{top}} \gamma_{\mathrm{bot}} e^{-2hH} \right)^n = \frac{1}{1 - \gamma_{\mathrm{top}} \gamma_{\mathrm{bot}} e^{-2hH}}\,. \tag{3.8}$$

Finally, we arrive at Theorem 3.2 for the truncation error of the image reflection series, which can be directly obtained by (3.5)–(3.8).

THEOREM 3.2. *If one truncates the image reflection series in (3.2) at $l = M$, the resulting U_M^{c} is an approximation of U^{c} with truncation error*

$$|U^{\mathrm{c}} - U_M^{\mathrm{c}}| \sim \mathcal{O}\left(|\gamma_{\mathrm{top}} \gamma_{\mathrm{bot}}|^{\lfloor \frac{M+1}{2} \rfloor} e^{-\frac{2\pi M H}{\max\{L_x, L_y\}}} \right). \tag{3.9}$$

Proof. By definition, one has

$$|U^{\mathrm{c}} - U_M^{\mathrm{c}}| = \frac{\pi}{L_x L_y} \sum_{i,j=1}^{N} q_i q_j {\sum_{\boldsymbol{h}}}' \frac{e^{-\iota \boldsymbol{h} \cdot \boldsymbol{r}_{ij}}}{h} \left[\beta_{ij}(h) - \beta_{ij}^M(h) \right], \tag{3.10}$$

where $\beta_{ij}^M(h)$ denotes the truncation of the image summation in (3.6) at $l = M$. When M is even, using the definitions of $\gamma_\pm^{(l)}$ and $z_{j\pm}^{(l)}$, one finds

$$\begin{aligned} \beta_{ij}(h) - \beta_{ij}^M(h) &= \sum_{l=M+1}^{\infty} \left[\gamma_+^{(l)} e^{-h\left|z_i - z_{j+}^{(l)}\right|} + \gamma_-^{(l)} e^{-h\left|z_i - z_{j-}^{(l)}\right|} \right] \\ &= \gamma_{\mathrm{top}}^{M/2} \gamma_{\mathrm{bot}}^{M/2} e^{-hMH} \beta_{ij}(h) \end{aligned} \tag{3.11}$$

by recursion. Similarly, if M is odd, one has

$$\beta_{ij}(h) - \beta_{ij}^{M}(h) = (\gamma_{\text{top}}\gamma_{\text{bot}})^{\frac{M+1}{2}}\, e^{-hMH}\left[e^{-h|H-z_{ij}|} + e^{-h|H+z_{ij}|} + e^{-hH}\beta_{ij}(h)\right]. \tag{3.12}$$

Note that U^{c} in (3.5) is well defined, $h \geq 2\pi/\max\{L_x, L_y\}$, and $|\beta_{ij}(h)| \leq (|\gamma_{\text{bot}}| + |\gamma_{\text{top}}| + |\gamma_{\text{bot}}\gamma_{\text{top}}|)/(1-\gamma_{\text{top}}\gamma_{\text{bot}}e^{-2hH})$. Substituting (3.11) and (3.12) into (3.10) and comparing with (3.5) lead us to (3.9). ∎

Theorem 3.2 provides two key insights: (1) When $|\gamma_{\text{top}}\gamma_{\text{bot}}| \ll 1$, the truncation error decreases exponentially in M as $|\gamma_{\text{top}}\gamma_{\text{bot}}|^{\frac{M+1}{2}}$; (2) the truncation error is significantly influenced by the aspect ratio of the system, i.e., $H/\max\{L_x, L_y\}$. For example, if $H \approx \max\{L_x, L_y\}$ and $|\gamma_{\text{top}}| = |\gamma_{\text{bot}}| = 1$, achieving an accuracy of 10^{-5} generally needs $M = 2$ levels of image reflections. However, if $H \ll \max\{L_x, L_y\}$, a much larger M must be chosen to guarantee the same accuracy.

In general, the number of reflection levels M required to achieve a desired tolerance ε can be estimated by

$$M \sim \frac{2\log\varepsilon - \log|\gamma_{\text{top}}\gamma_{\text{bot}}|}{\log|\gamma_{\text{top}}\gamma_{\text{bot}}| - \frac{4\pi H}{\max\{L_x, L_y\}}}\,, \tag{3.13}$$

which is a direct consequence of (3.9). Equation (3.13) also explains the conflicting conclusions made in literature. In [13], a very large aspect ratio is chosen, so that $M = 50$ is needed, while in [66], $H = \max\{L_x, L_y\}/3$, where choosing $M = 5$ can already provide 5-digit accuracy according to (3.13).

3.3. Efficient summation formula for dielectrically confined quasi-2D systems. Upon truncating the image reflection series at $l = M$, the resulting system, referred to as Ω_{Q2D}^{M}, can be considered a homogeneous quasi-2D system with a height of $\hat{L}_M = (2M+1)H$. Thus one can analogously obtain its corresponding IBC and ELC corrections as was discussed in section 2.2.

First, the energy U^{c} can be decomposed via Ewald-splitting:

$$U^{\text{c}} \approx U_M^{\text{c}} = U_{\text{real}}^{\text{c}} + U_{\text{Fourier}}^{\text{c}}, \tag{3.14}$$

where the real space component $U_{\text{real}}^{\text{c}}$ is given by

$$\begin{aligned} U_{\text{real}}^{\text{c}} = \frac{1}{2}\sum_{i,j=1}^{N} q_i q_j \Bigg[{\sum_{\boldsymbol{n}}}' \frac{\operatorname{erfc}(\alpha\,|\boldsymbol{r}_{ij}+\boldsymbol{\ell}|)}{|\boldsymbol{r}_{ij}+\boldsymbol{\ell}|} + \sum_{\boldsymbol{n}}\sum_{l=1}^{M} \frac{\gamma_+^{(l)}\operatorname{erfc}\left(\alpha\left|\boldsymbol{r}_i - \boldsymbol{r}_{j+}^{(l)} + \boldsymbol{\ell}\right|\right)}{\left|\boldsymbol{r}_i - \boldsymbol{r}_{j+}^{(l)} + \boldsymbol{\ell}\right|} \\ + \sum_{\boldsymbol{n}}\sum_{l=1}^{M} \frac{\gamma_-^{(l)}\operatorname{erfc}\left(\alpha\left|\boldsymbol{r}_i - \boldsymbol{r}_{j-}^{(l)} + \boldsymbol{\ell}\right|\right)}{\left|\boldsymbol{r}_i - \boldsymbol{r}_{j-}^{(l)} + \boldsymbol{\ell}\right|} \Bigg]. \end{aligned} \tag{3.15}$$

In (3.15), the additional terms compared to (2.6) represent the interaction between the actual charges and the fictitious image charges; the detailed formula for the real space component of force is given by (SM1.3) in the supplementary material. The $\boldsymbol{k}$-space component $U_{\text{Fourier}}^{\text{c}}$ is given by

$$U_{\text{Fourier}}^{\text{c}} = \frac{1}{2\alpha L_x L_y}\sum_{i,j=1}^{N} q_i q_j {\sum_{\boldsymbol{h}}}' e^{\iota\boldsymbol{h}\cdot\boldsymbol{r}_{ij}} \int_{-\infty}^{\infty} \frac{e^{-\frac{h^2}{4\alpha^2}-t^2}}{\frac{h^2}{4\alpha^2}+t^2}\Gamma_{ij}(t)dt - \frac{\alpha}{\sqrt{\pi}}\sum_{i=1}^{N} q_i^2 + \mathcal{J}_0\,, \tag{3.16}$$

where

$$\Gamma_{ij}(t) := e^{2\iota\alpha z_{ij}t} + \sum_{l=1}^{\infty}\left[\gamma_+^{(l)} e^{2\iota\alpha t(z_i - z_{j+}^{(l)})} + \gamma_-^{(l)} e^{2\iota\alpha t(z_i - z_{j-}^{(l)})}\right] \tag{3.17}$$

and the **0**th mode correction $\mathcal{J}_0$ reads

$$\mathcal{J}_0 = \frac{1}{2\alpha L_x L_y}\sum_{i,j=1}^{N} q_i q_j \int_{-\infty}^{\infty} \frac{e^{-t^2}\Gamma_{ij}(t) - \Gamma_{ij}(0)}{t^2} dt. \tag{3.18}$$

By further employing the trapezoidal rule to discretize the integrals, we derive an efficient summation formula accompanied by error estimates, as detailed in Theorem 3.3.

THEOREM 3.3. *Assume $L_z > H$; discretizing the integrals in* (3.16) *via the trapezoidal rule with mesh size $\pi/\alpha L_z$, one has*

$$U^{\mathrm{c}}_{\mathrm{Fourier}} = \frac{2\pi}{L_x L_y L_z}\sum_{\boldsymbol{k}}{}' \frac{e^{-\frac{k^2}{4\alpha^2}}}{k^2}\rho_{\boldsymbol{k}}\bar{\rho}^M_{\boldsymbol{k}} - \frac{\alpha}{\sqrt{\pi}}\sum_{i=1}^{N} q_i^2 + U^M_{\mathrm{IBC}} + U^M_{\mathrm{ELC}} + U^M_{\mathrm{err}}, \tag{3.19}$$

where $\boldsymbol{k} = 2\pi(n_x/L_x, n_y/L_y, n_z/L_z)$, the structure factors $\rho_{\boldsymbol{k}}$ and $\bar{\rho}^M_{\boldsymbol{k}}$ are defined by

$$\rho_{\boldsymbol{k}} := \sum_{i=1}^{N} q_i e^{\iota\boldsymbol{k}\cdot\boldsymbol{r}_i} \quad \textit{and} \quad \bar{\rho}^M_{\boldsymbol{k}} := \sum_{j=1}^{N} q_j\left[e^{-\iota\boldsymbol{k}\cdot\boldsymbol{r}_j} + \sum_{l=1}^{M}\left(\gamma_+^{(l)} e^{-\iota\boldsymbol{k}\cdot\boldsymbol{r}_{j+}^{(l)}} + \gamma_-^{(l)} e^{-\iota\boldsymbol{k}\cdot\boldsymbol{r}_{j-}^{(l)}}\right)\right], \tag{3.20}$$

the second term on the RHS is the self-energy correction,

$$U^M_{\mathrm{IBC}} := \frac{2\pi}{L_x L_y L_z}\left(\sum_{i=1}^{N} q_i z_i\right)\sum_{j=1}^{N} q_j\left[z_j + \sum_{l=1}^{M}\left(\gamma_+^{(l)} z_{j+}^{(l)} + \gamma_-^{(l)} z_{j-}^{(l)}\right)\right], \tag{3.21}$$

$$U^M_{\mathrm{ELC}} := \frac{2\pi}{L_x L_y}\sum_{i,j=1}^{N} q_i q_j \sum_{\boldsymbol{h}}{}' \frac{e^{\iota\boldsymbol{h}\cdot\boldsymbol{r}_{ij}}}{h}\frac{\cosh(hz_{ij}) + \mathcal{G}_{ij}(h)}{1 - e^{hL_z}} \tag{3.22}$$

are the corresponding IBC and ELC correction terms with

$$\mathcal{G}_{ij}(h) := \sum_{l=1}^{M}\left[\gamma_+^{(l)}\cosh(h(z_i - z_{j+}^{(l)})) + \gamma_-^{(l)}\cosh(h(z_i - z_{j-}^{(l)}))\right], \tag{3.23}$$

and U^M_{err} is the remainder error term. The last two terms have decay rates

$$\left|U^M_{\mathrm{ELC}}\right| \sim \mathcal{O}\left(e^{-\frac{2\pi(L_z - H)}{\max\{L_x, L_y\}}} + \sum_{l=1}^{M}\left[\gamma_+^{(l)} + \gamma_-^{(l)}\right] e^{-\frac{2\pi(L_z - (2\lceil l/2\rceil + 1)H)}{\max\{L_x, L_y\}}}\right) \tag{3.24}$$

and

$$\left|U^M_{\mathrm{err}}\right| \sim \mathcal{O}\left(e^{-\alpha^2(L_z - H)^2} + \sum_{l=1}^{M}\left(\gamma_+^{(l)} + \gamma_-^{(l)}\right) e^{-\alpha^2(L_z - (2\lceil l/2\rceil + 1)H)^2}\right), \tag{3.25}$$

respectively.

Proof. Analogous to the proof of Theorem 2.1, by error analysis for the trapezoidal rule as outlined in Appendix A, it can be shown that the quadrature discretization of (3.16) directly yields the first two terms in (3.19), as well as the residual correction associated with the ELC term. The estimates for both the ELC term and the remainder error term can be derived using the results in Theorem 2.1. Suppose that $\mathcal{G}_{ij}^{(l)}(h) := \gamma_+^{(l)} \cosh(h(z_i - z_{j+}^{(l)})) + \gamma_-^{(l)} \cosh(h(z_i - z_{j-}^{(l)}))$. For the ELC term, one observes that

$$\mathcal{G}_{ij}^{(l)}(h) \sim \left(\gamma_+^{(l)} + \gamma_-^{(l)}\right) e^{lhH} \cosh(hz_{ij}) \qquad \text{if } l \text{ is even}, \tag{3.26}$$

and

$$\begin{aligned} \mathcal{G}_{ij}^{(l)}(h) &= \gamma_+^{(l)} \cosh(h(z_i + z_j - (l+1)H)) + \gamma_-^{(l)} \cosh(h(z_i + z_j + (l-1)H)) \\ &= \frac{e^{lhH}}{2} \Bigg[e^{hz_{ij}+2hz_j} \left(\gamma_+^{(l)} e^{-(2l+1)hH} + \gamma_-^{(l)} e^{-hH}\right) \\ &\quad + e^{-hz_{ij}-2hz_j} \left(\gamma_+^{(l)} e^{hH} + \gamma_-^{(l)} e^{-(2l-1)hH}\right) \Bigg] \\ &\sim \left(\gamma_+^{(l)} + \gamma_-^{(l)}\right) e^{(l+1)hH} \cosh(hz_{ij}) \end{aligned} \tag{3.27}$$

if l is odd. Substituting (3.26) and (3.27) into (3.23) yields

$$\mathcal{G}_{ij}(h) \sim \cosh(hz_{ij}) \sum_{l=1}^{M} \left(\gamma_+^{(l)} + \gamma_-^{(l)}\right) e^{2\lceil l/2 \rceil hH}. \tag{3.28}$$

Substituting this result into (3.22) and using (2.16), one finds that

$$\begin{aligned} \left|U_{\mathrm{ELC}}^{M}\right| &\sim \left[1 + \sum_{l=1}^{M} \left(\gamma_+^{(l)} + \gamma_-^{(l)}\right) e^{2\lceil l/2 \rceil hH}\right] |U_{\mathrm{ELC}}| \\ &= \mathcal{O}\left(e^{-\frac{2\pi(L_z - H)}{\max\{L_x, L_y\}}} + \sum_{l=1}^{M} \left[\gamma_+^{(l)} + \gamma_-^{(l)}\right] e^{-\frac{2\pi(L_z - (2\lceil l/2 \rceil + 1)H)}{\max\{L_x, L_y\}}}\right). \end{aligned} \tag{3.29}$$

An estimate for the remainder error term can be derived similarly. ∎

It should be noted that, in contrast to the homogeneous case, here the first two terms on the RHS are no longer identical to that of the standard Ewald3D summation, since now the charged system consists of both real charges and fictitious image charges.

Finally, based on Theorem 3.3, we obtain the following criterion for selecting appropriate values of M and L_z to ensure that the contributions from the image truncation error, the ELC term, and the remainder error term are all below a specified tolerance ε:

- First, choose the image reflection truncation level M according to (3.13), such that $|U^{\mathrm{c}} - U_M^{\mathrm{c}}| \le \varepsilon$.
- Second, choose the extended height of the domain L_z according to (3.24)–(3.25), such that both $\left|U_{\mathrm{ELC}}^{M}\right| \le \varepsilon$ and $\left|U_{\mathrm{err}}^{M}\right| \le \varepsilon$ are satisfied.

In the worst-case scenario where $|\gamma_{\mathrm{top}}| = |\gamma_{\mathrm{bot}}| = 1$, the decay rates of $|U_{\mathrm{ELC}}^{M}|$ and $|U_{\mathrm{err}}^{M}|$ are solely determined by the exponential factors, as evident from (3.24) and (3.25). It is found that L_z can be chosen according to

$$L_z \ge (M+1)H + \max\left\{\frac{\max\{L_x, L_y\}}{2\pi} \log\frac{1}{\varepsilon},\ \frac{1}{\alpha}\sqrt{\log\frac{1}{\varepsilon}}\right\}. \tag{3.30}$$

Particularly, it is observed that L_z needs to be larger than $(M+1)H$; this can be understood as a physical constraint which prevents the z-replicas of actual charges overlapping with their image charges. Equation (3.30) also explains the counterintuitive convergence result in [66], where it was observed that increasing M (while keeping L_z fixed) may lead to a nonmonotonic behavior in accuracy; i.e., the error first decays as M increases but eventually grows exponentially when M is large. It can now be understood that if one keeps increasing M but with L_z fixed, then the constraint $L_z \geq (M+1)H$ will eventually be violated, and then the approximation is no longer stable.

3.4. RBE2D method for dielectrically confined quasi-2D systems. We now extend the RBE2D method for efficient MD simulations of dielectrically confined quasi-2D Coulomb systems. First, given tolerance ε, one shall choose appropriate values for M and L_z, such that the image series truncation error, the ELC term, and remainder error term can all be neglected. Then, let $\boldsymbol{F}^{\mathrm{c}}_{\mathrm{Fourier}}$ denote the $\boldsymbol{k}$-space component of force acting on the ith particle; it reads

$$\boldsymbol{F}^{\mathrm{c}}_{\mathrm{Fourier}}(\boldsymbol{r}_i) = -\frac{2\pi}{L_x L_y L_z} {\sum_{\boldsymbol{k}}}' \frac{e^{-\frac{k^2}{4\alpha^2}}}{k^2} \nabla_{\boldsymbol{r}_i} \left[\rho_{\boldsymbol{k}} \bar{\rho}^M_{\boldsymbol{k}}\right] + \boldsymbol{F}^M_{\mathrm{IBC}}(\boldsymbol{r}_i)\,, \tag{3.31}$$

where

$$\begin{aligned} \nabla_{\boldsymbol{r}_i} \left[\rho_{\boldsymbol{k}} \bar{\rho}^M_{\boldsymbol{k}}\right] = q_i \boldsymbol{k} \mathrm{Im} &\left[e^{-\iota \boldsymbol{k}\cdot\boldsymbol{r}_i} \left(\rho_{\boldsymbol{k}} + \rho^M_{\boldsymbol{k}}\right) + \sum_{\substack{l=1 \\ \text{even}}}^{M} \left(\gamma^{(l)}_+ e^{-\iota \boldsymbol{k}\cdot\boldsymbol{r}^{(l)}_{i+}} + \gamma^{(l)}_- e^{-\iota \boldsymbol{k}\cdot\boldsymbol{r}^{(l)}_{i-}}\right) \rho_{\boldsymbol{k}} \right] \\ + q_i \widehat{\boldsymbol{k}} \mathrm{Im} &\left[\sum_{\substack{l=1 \\ \text{odd}}}^{M} \left(\gamma^{(l)}_+ e^{-\iota \boldsymbol{k}\cdot\boldsymbol{r}^{(l)}_{i+}} + \gamma^{(l)}_- e^{-\iota \boldsymbol{k}\cdot\boldsymbol{r}^{(l)}_{i-}}\right) \rho_{\boldsymbol{k}} \right] \end{aligned} \tag{3.32}$$

with $\rho^M_{\boldsymbol{k}}$ the conjugate of $\bar{\rho}^M_{\boldsymbol{k}}$ and $\widehat{\boldsymbol{k}} = (k_x, k_y, -k_z)$. The calculation of (3.31) can also be accelerated via FFT, namely, the ICM-PPPM method [66], which combines the image charge method (ICM) with PPPM. If the image reflection level is truncated at M, the computational cost of ICM-PPPM is $\mathcal{O}(MN\log(MN))$. Thus for strongly confined systems, the cost of the FFT-based method will increase rapidly as M increases.

We now again apply the importance sampling technique to approximate $\boldsymbol{F}^{\mathrm{c}}_{\mathrm{Fourier}}$, yielding the following stochastic estimator:

$$\boldsymbol{F}^{\mathrm{c}}_{\mathrm{Fourier}}(\boldsymbol{r}_i) \approx \boldsymbol{F}^{\mathrm{c},*}_{\mathrm{Fourier}}(\boldsymbol{r}_i) = -\frac{2\pi}{L_x L_y L_z} \sum_{\ell=1}^{P} \frac{S}{P} \frac{\nabla_{\boldsymbol{r}_i} \left[\rho_{\boldsymbol{k}_\ell} \bar{\rho}^M_{\boldsymbol{k}_\ell}\right]}{k_\ell^2} + \boldsymbol{F}^M_{\mathrm{IBC}}(\boldsymbol{r}_i), \tag{3.33}$$

where $\{\boldsymbol{k}_\ell\}_{\ell=1}^P$ are the P batches of wave vectors sampled from $\mathscr{P}(\boldsymbol{k})$. It is important to note that when surface charges are present at the interfaces [55, 64, 66], a straightforward modification to (3.33) is required, which allows for the simultaneous treatment of discrete ions and continuous surface charges. Detailed information can be found in the supplementary material section SM1. And the real space component of force is given by (SM1.3), which can still be evaluated by neighbor lists algorithms.

Next, we describe a simple strategy for efficiently summing over the $2MN$ image charges. Notice that (3.32) can be rewritten as

$$\begin{aligned}\nabla_{\boldsymbol{r}_i}\left[\rho_{\boldsymbol{k}}\bar{\rho}_{\boldsymbol{k}}^M\right] &= q_i\boldsymbol{k}\mathrm{Im}\left[e^{-\iota\boldsymbol{k}\cdot\boldsymbol{r}_i}\sum_{j=1}^N q_j e^{\iota\boldsymbol{k}\cdot\boldsymbol{r}_j}\left(1+e^{-2\iota k_z z_j}Y_{\mathrm{odd}}(k_z)+Y_{\mathrm{even}}(k_z)\right)\right]\\ &+ q_i\boldsymbol{k}\mathrm{Im}\left[e^{-\iota\boldsymbol{k}\cdot\boldsymbol{r}_i}\left(1+e^{2\iota k_z z_i}\overline{Y}_{\mathrm{odd}}(k_z)\right)\rho_{\boldsymbol{k}}\right]+q_i\widehat{\boldsymbol{k}}\mathrm{Im}\left[e^{-\iota\boldsymbol{k}\cdot\boldsymbol{r}_i}\overline{Y}_{\mathrm{even}}(k_z)\rho_{\boldsymbol{k}}\right],\end{aligned}\tag{3.34}$$

where the coefficients Y_{odd} and Y_{even} are defined as follows:

$$\begin{aligned}Y_{\mathrm{odd}}(k_z) &= \sum_{l=1,\mathrm{odd}}^M\left[\gamma_+^{(l)}e^{\iota k_z(l+1)H}+\gamma_-^{(l)}e^{-\iota k_z(l-1)H}\right],\\ Y_{\mathrm{even}}(k_z) &= \sum_{l=1,\mathrm{even}}^M\left[\gamma_+^{(l)}e^{\iota k_z lH}+\gamma_-^{(l)}e^{-\iota k_z lH}\right].\end{aligned}\tag{3.35}$$

This formulation enables the decoupling of the summation over the particles' index j and their image index l. In practical simulations, one shall first precompute $Y_{\mathrm{odd}}(k_z)$ and $Y_{\mathrm{even}}(k_z)$ for each $\boldsymbol{k}\in\{\boldsymbol{k}_\ell\}_{\ell=1}^P$, as these are configuration independent, with a computational cost of $\mathcal{O}(PM)$. Subsequently, for a given particle configuration, one evaluates $\rho_{\boldsymbol{k}}$, along with the conjugates of Y_{odd} and Y_{even}, and computes

$$\sum_{j=1}^N q_j e^{\iota\boldsymbol{k}\cdot\boldsymbol{r}_j}\left(1+e^{-2\iota k_z z_j}Y_{\mathrm{odd}}(k_z)+Y_{\mathrm{even}}(k_z)\right)\tag{3.36}$$

for every $\boldsymbol{k}\in\{\boldsymbol{k}_\ell\}_{\ell=1}^P$, which incurs a cost of $\mathcal{O}(PN)$ operations. These intermediate variables are then utilized to evaluate $\nabla_{\boldsymbol{r}_i}\left[\rho_{\boldsymbol{k}}\bar{\rho}_{\boldsymbol{k}}^M\right]$ for all particles i using (3.34), adding another $\mathcal{O}(PN)$ to the cost. Finally, substituting the value of $\nabla_{\boldsymbol{r}_i}\left[\rho_{\boldsymbol{k}}\bar{\rho}_{\boldsymbol{k}}^M\right]$ into (3.33) allows for the computation of the first term on the RHS with $\mathcal{O}(PN)$ operations, followed by the addition of the IBC term, which incurs an $\mathcal{O}(N)$ cost. Consequently, the total computational cost for force evaluations is reduced from $\mathcal{O}(PMN)$ to $\mathcal{O}(P(M+N))$. In practice, one shall still take $\alpha\sim N^{1/3}/(L_xL_yH)^{1/3}$ to ensure that the real space calculation costs $\mathcal{O}(N)$; then the $\boldsymbol{k}$-space components of force can be calculated as such so that the complexity is reduced to $\mathcal{O}(P(M+N))$. Thus, the overall complexity of the RBE2D is approximately $\mathcal{O}(N)$ since both P and M are of $\mathcal{O}(1)$ and independent of N. The detailed algorithm for RBE2D accelerated MD in the presence of dielectric interfaces is summarized in Algorithm 3.1.

Finally, consider the fluctuation of random batch approximation of the force, denoted as $\boldsymbol{\Xi}_{\boldsymbol{F},i}^{\mathrm{c}}=\boldsymbol{F}_{\mathrm{Fourier}}^{\mathrm{c},*}(\boldsymbol{r}_i)-\boldsymbol{F}_{\mathrm{Fourier}}^{\mathrm{c}}(\boldsymbol{r}_i)$; one can still show that (1) the variance of the RBE2D method is controlled via $\mathcal{O}(1/P)$ and is independent of L_z; (2) the RBE2D is capable of capturing finite time structure and dynamic properties in MD simulations. The proof is similar to Theorems 2.3 and 2.4 and is thus omitted here.

4. Numerical results on quasi-2D systems without dielectric interfaces. In this section, numerical results are first presented for the homogeneous case, validating the performance of RBE2D accelerated MD simulations. Examples include coarse-grained models of electrolytes and all-atom SPC/E bulk water systems [6] confined by two slabs without dielectric jumps, where all the quantities are defined and calculated in reduced LJ units and real units [18], respectively. Our method is implemented in LAMMPS (version 29Oct2020) [56] and performed on the "Siyuan Mark-I" high performance cluster at Shanghai Jiao Tong University. Each node is equipped with 2× Intel Xeon ICX Platinum 8358 CPU (2.6GHz, 32 cores) and 512 GB memory. The code is highly optimized, where the message passing interface (MPI) and Intel AVX-512 instructions are used for parallelization and vectorization, respectively.

Algorithm 3.1 (RBE2D for quasi-2D systems under dielectric confinement).

1: Choose α, r_c (the cutoff in real space), Δt, batch size P, image reflection level of truncation M, and the vacuum layer parameter L_z. Initialize the coefficients of dielectric jumps (ε_{top}, ε_{c}, ε_{bot}) and the positions and velocities of charges $\boldsymbol{r}_i^0, \boldsymbol{v}_i^0$ for $1 \le i \le N$. Set N_T as the total MD time steps.
2: **for** n in $1 : N_T$ **do**
3: Sample P nonzero frequencies $\boldsymbol{k} \sim e^{-k^2/(4\alpha)}$ by the Metropolis procedure to form set $\mathcal{K}$.
4: The real space component of force is computed via a neighbor list algorithm (for both actual charges and image charges within r_c).
5: The Fourier space component of the force is computed via the random batch approximation $\boldsymbol{F}^{\text{c},*}_{\text{Fourier}}$, with P frequencies from the set $\mathcal{K}$.
6: Integrate the equations of motion for time Δt with an appropriate integration scheme and some appropriate thermostat.
7: **end for**

To benchmark the accuracy, several widely investigated quantities are computed, such as concentration, mean-squared displacement (MSD), velocity auto-correlation functions (VACFs), ensemble-averaged energy distribution, etc. The calculation methods for these quantities are described in section SM2 of the supplementary material. For comparison, we used the stable implementation of the PPPM2D method [8] provided inside LAMMPS. Results obtained using the PPPM2D method are labeled as "PPPM." The parameters of the PPPM were automatically chosen in LAMMPS to achieve a desired relative error of $\Delta = 10^{-4}$ for force evaluations [10]. To allow a fair comparison, the Ewald-splitting parameter α is always set to be the same for RBE2D and PPPM methods.

4.1. Accuracy test case I: 3:1 electrolytes immersed in an implicit solvent. We first perform coarse-grained MD simulations of $3:1$ electrolytes in the NVT ensemble. Following the primitive model, all the ions are represented as soft spheres of diameter σ and mass m that interact via electrostatic interactions and a purely repulsive shifted-truncated LJ potential

$$U_{\text{LJ}} = \begin{cases} 4\varepsilon_{\text{LJ}} \left[\left(\dfrac{\sigma}{r_{ij}} \right)^{12} - \left(\dfrac{\sigma}{r_{ij}} \right)^{6} + \dfrac{1}{4} \right], & r_{ij} \le r_{\text{LJ}}, \\ 0, & r_{ij} > r_{\text{LJ}}, \end{cases} \tag{4.1}$$

where r_{ij} is the distance between the ith and jth particles, $r_{\text{LJ}} = 2^{1/6}\sigma$ is the LJ truncation distance, $\varepsilon_{\text{LJ}} = k_{\text{B}}T$ is the coupling strength, k_{B} is the Boltzmann constant, and T is the temperature. These ions are immersed in a continuum solvent, characterized by a Bjerrum length $\ell_{\text{B}} = e^2/(4\pi\varepsilon_c k_{\text{B}}T) = 3.5\sigma$. The system has dimensions $L_x = 90\sigma$, $L_y = 90\sigma$, and $H = 30\sigma$, containing 750 cations and 2250 anions. The ions are confined in z by purely repulsive LJ walls at $z = 0$ and $z = 30\sigma$, with parameters $\varepsilon_{\text{wall}} = \varepsilon_{\text{LJ}}$ and $\sigma_{i,\text{wall}} = 0.5\sigma$. The initial 10^6 steps with $\Delta t = 10^{-3}\tau$ are performed for equilibrium, where $\tau = \sqrt{m\sigma^2/\varepsilon_{\text{LJ}}}$ denotes the LJ unit of time. The production phase follows for another 10^7 steps, and the configurations are sampled every 100 time steps for statistics. The temperature is maintained by using a Nosé–Hoover thermostat [23] with relaxation times 0.01τ, and r_c is set as 10σ for both the RBE2D and PPPM methods.

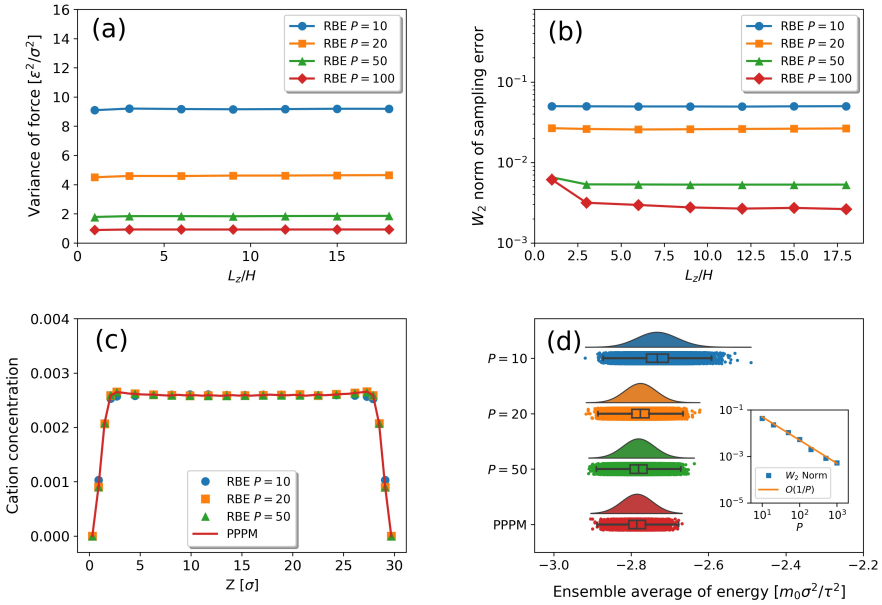

FIG. 2. *MD results for* 3 : 1 *electrolytes.* (a)–(b) *Variance of force and the error on ensemble average of the potential energy as a function of the relative size of the extended system,* L_z/H. (c) *Concentration of cations along* z*-dimension.* (d) *Raincloud plots of the ensemble average distribution of the potential energy as well as a boxplot and raw data-points. In* (a), (c), *and* (d), *results are shown for the RBE2D with different batch sizes* P *and the PPPM. In* (b), *we use the* W_2 *norm defined in* (4.2) *to measure the difference between two distributions. The inset in* (d) *shows the convergence on the* W_2 *norm with* $\mathcal{O}(1/P)$ *rate.*

First, we consider the ensemble average of the variance in forces, denoted as $\langle \|\mathbb{E}|\boldsymbol{\Xi}_i|^2\|_\infty \rangle$, as shown in Figure 2(a). Clearly, the force variance is independent of the vacuum layer thickness parameter L_z, which validates our theoretical result stated in Theorem 2.3. Then we compared the distributions of the potential energy of the obtained samples by the RBE2D and PPPM methods, denoted as $\mathscr{P}_{\mathrm{RBE}}(\boldsymbol{x})$ and $\mathscr{P}_{\mathrm{PPPM}}(\boldsymbol{y})$, respectively. The Wasserstein-2 norm [53, 32] is used to measure the difference between two distributions, defined as

$$W_2(\mathscr{P}_{\mathrm{RBE}}, \mathscr{P}_{\mathrm{PPPM}}) = \left(\inf_{\gamma \in \Pi(\mathscr{P}_{\mathrm{RBE}}, \mathscr{P}_{\mathrm{PPPM}})} \int |\boldsymbol{x} - \boldsymbol{y}|^2 d\gamma(\boldsymbol{x}, \boldsymbol{y}) \right)^{1/2}, \tag{4.2}$$

where $\Pi(\mathscr{P}_{\mathrm{RBE}}, \mathscr{P}_{\mathrm{PPPM}})$ represents the set of all joint distributions with marginal distributions $\mathscr{P}_{\mathrm{RBE}}$ and $\mathscr{P}_{\mathrm{PPPM}}$. The corresponding results are shown Figure 2(b), where the W_2 norms are plotted as functions of L_z/H with varying batch size P. According to Theorem 2.1, when $L_z \approx H$, the errors coming from the ELC and remainder error term are still large and cannot be ignored; this is consistent with the error decay observed here. We also find that, as $L_z \geq 3H$, the error no longer decreases as L_z/H increases (with P fixed), indicating that both ELC and the remainder error terms now indeed become negligible, and the error primarily comes from the random batch approximation.

Finally, the concentration of trivalent ions along z and the distribution of energy are investigated. The corresponding results are depicted in Figure 2(c–d). We observe a convergence rate of $\mathcal{O}(1/P)$ in the average energy by the RBE2D (with

that of the PPPM set as benchmark value). This is consistent with our theoretical prediction Theorem 2.3 as the energies of both Coulomb and LJ scale quadratically in displacement near equilibrium. It is also noticed that, for the RBE2D method, choosing $P = 50$ can already yield very accurate results, which are almost indistinguishable from those obtained via PPPM. Theorem 2.4 also indicates that the error bound in the potential energy of the RBE2D method should converge linearly in Δt. As numerically validated in Figure SM1 in the supplementary material, the error indeed decays with $\mathcal{O}(\Delta t)$ scaling. However, this $\mathcal{O}(\Delta t)$ scaling may not hold when Δt is larger or in more complicated molecular models. In those scenarios, increasing Δt can lead to particles coming very close to one another (even with the presence of the LJ potential), introducing additional sources of error in other MD components—particularly in managing bond, angle, and dihedral constraints [18]. These artificial effects may result in unphysically large forces or even cause the simulation to fail.

4.2. Accuracy test case II: All-atom SPC/E bulk water system. Next, we perform MD simulations for the SPC/E bulk water system [6]. The system has dimensions $L_x = L_y = H = 55.9$ Å and consists of 17496 atoms. Two purely repulsive shifted-truncated LJ walls (with $\varepsilon_{\text{atom-wall}} = k_{\text{B}}T$) are located at $z = 0$ and $z = H$. The simulations utilize a time step $\Delta t = 1fs$, and T is fixed at $298K$ by an NH thermostat with relaxation time $10fs$. Equilibration proceeds for 10^5 time steps, followed by a 10^6-step production period, with configurations sampled every 100 time steps. The cutoff is set as $r_c = 10\mathring{A}$, and the ratio L_z/H is fixed as 3 to ensure that both the ELC and the remainder error term are negligible.

We analyze various equilibrium and dynamic properties of the system, including the oxygen concentration, the MSD in z, the VACF, and the distribution of potential energy U. The results are summarized in Figure 3(a-d). Notably, the RBE2D method yields highly consistent results in comparison to the PPPM method across all examined properties when $P \geq 100$. This underscores RBE2D's ability to effectively capture spatiotemporal information across multiple scales in molecular dynamics simulations.

4.3. CPU time performance. We now report the CPU time performance of the RBE2D method, compared to the PPPM method. The SPC/E bulk water systems are simulated, where the system dimensions are set as $L_x = L_y = H$, and the system size changes as one varies N with the density of water being fixed at $1g/cm^3$. For a fair comparison, a cutoff of $10\mathring{A}$ and a relative error threshold of 10^{-4} are set for both methods.

We first investigate the time cost and complexity by varying particle number N. In Figure 4(a), 64 CPU cores are used, and the CPU time per MD step for the RBE2D and the PPPM methods is documented with particle number N up to 2×10^6, where the real space CPU cost is identical for both methods by fixing the same Ewald-splitting parameter α and real space cutoff r_c. It should be noted that the main goal of such a parameter choice is solely comparing the improvement of the RBE2D in Fourier space. We expect that a fine tuning of α and other parameters to balance the cost of RBE2D in real and Fourier spaces can further optimize its efficiency in practice. The results clearly demonstrate the $\mathcal{O}(N)$ complexity of the RBE2D method and its significant advantage over the PPPM method in the Fourier space computation. A more detailed comparison is further provided in Figure SM4 in the supplementary material, where we compared the performance of each component of the RBE2D and PPPM methods with CPU cores fixed to be both 64 and 1024. The results show the improvement of the RBE2D method in the Fourier component

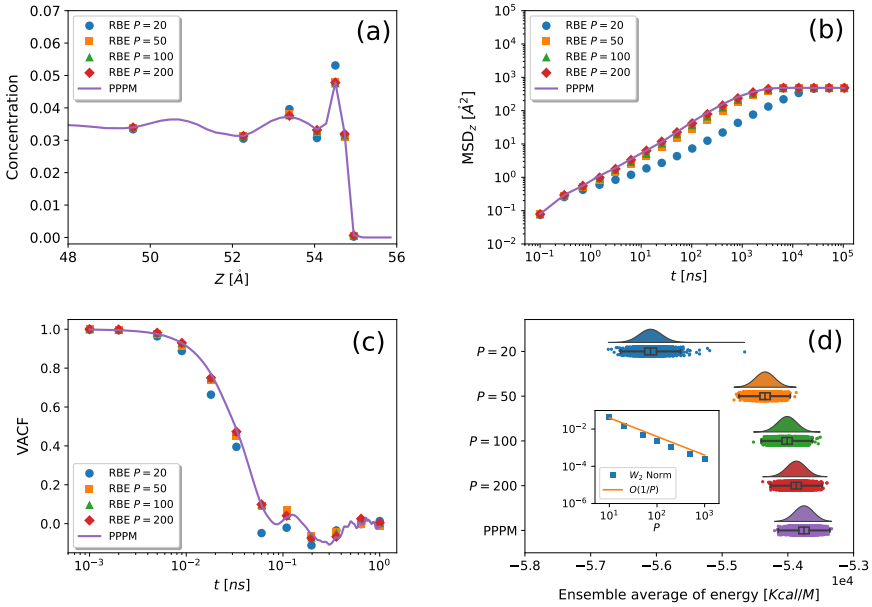

FIG. 3. *MD results for an SPC/E bulk water system.* (a) *Concentration of oxygen near the top surface;* (b) *MSD along z-direction;* (c) *VACF; and* (d) *raincloud plots of the ensemble average distribution of the potential energy as well as a boxplot and raw data-points. The RBE2D with different batch sizes P and the PPPM are plotted. The inset in* (d) *shows the convergence on the W_2 norm with $\mathcal{O}(1/P)$ rate.*

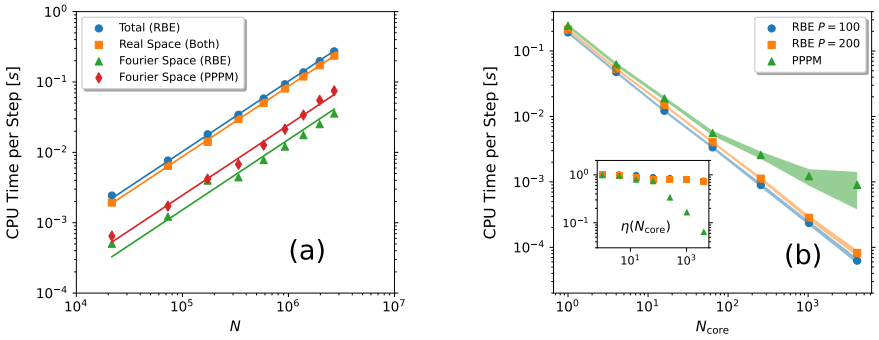

FIG. 4. (a) *CPU time per step for the RBE2D method and PPPM method with increasing N and* (b) *total CPU time for comparison between the RBE2D and the PPPM with the number of CPU cores N_{core} up to* 1024. *The results in* (a) *are obtained with* 64 *cores and $P=100$, where the real space cost is identical for both methods by fixing the same Ewald splitting parameter α and real space cutoff r_c. The solid lines indicate linear scaling. In* (b)*, data is shown for the RBE2D with batch size $P=100$ and $P=200$ and the PPPM, where the light-colored parts stand for the range of error bar. The inset in* (b) *shows the strong parallel efficiency $\eta(N_{\mathrm{core}})$.*

computation across the entire range of particle numbers N, especially when utilizing a larger number of CPU cores.

Next, we compare the RBE2D and PPPM methods, in terms of both CPU time performance and parallel scalability. Let N_{core} be the number of cores utilized and $T(N_{\mathrm{core}})$ the corresponding CPU time. The parallel efficiency for a strong scaling experiment is defined as

$$\eta(N_{\text{core}}) = \frac{N_{\min}}{N_{\text{core}}} \frac{T_{\min}}{T(N_{\text{core}})}, \tag{4.3}$$

where $T_{\min} = T(N_{\min})$ and $N_{\min}$ is the minimal number of CPUs used. Figure 4(b) and its inset document the CPU time and strong scaling results by the RBE2D and PPPM methods for a system comprising 139968 atoms. Clearly, the two methods perform similarly when N_{core} is small, and RBE2D outperforms PPPM as N_{core} increases; the advantage becomes significant for $N_{\text{core}} > 64$. Notably, when $N_{\text{core}} \geq 1024$, RBE2D is approximately 10 times faster than PPPM. Furthermore, the strong scaling of RBE2D remains over 70% when ~ 4000 CPUs are employed, while that of the PPPM drops rapidly to 6%. The main difference between these two methods lies in their communication cost. RBE2D requires only a single global communication for the reduction of P structure factors. In comparison, the PPPM method, due to its use of FFT, requires six sequential rounds of communication to perform both forward and backward Fourier transforms, leading to poor scalability [5, 3]. This highlights the excellent parallel scalability of the RBE2D method.

5. Numerical results on quasi-2D systems under dielectric confinement. In this section, numerical simulations are performed for systems in the presence of dielectric interfaces, including dielectrically confined electrolytes and SPC/E bulk water, to further validate the RBE2D method. Reduced LJ units and real units are used to parameterize these systems, respectively. As a benchmark for accuracy and efficiency, the simulations are also conducted using the HSMA method [39] and the ICM-PPPM method [66]; both have been implemented in LAMMPS [40]. For the RBE2D, parameters such as M and L_z are selected according to section 3.3, while for the HSMA and ICM-PPPM, we use the same parameters suggested by [39] and [66], respectively. For all methods, the threshold in relative errors is set to 10^{-4}.

5.1. Accuracy test case III: Dielectrically confined electrolytes. Here we examine four distinct electrolyte systems that are confined by two dielectric interfaces. These systems include 2:1 and 3:1 electrolytes with varying surface charge densities and dielectric contrasts. In these systems, all ions are modeled as soft spheres of diameter r_{d}, and are confined by purely repulsive shifted-truncated LJ walls ($\varepsilon_{\text{ion-wall}} = k_{\text{B}}T$; $\sigma_{\text{ion-wall}} = 0.5r_{\text{d}}$) at $z = 0$ and $z = H$. More detailed information regarding the system settings can be found in Table SM1 in the supplementary material. The MD simulations utilize a time step 0.005τ, with temperature controlled by an NH thermostat with a damping time of 0.05τ, where τ is the reduced LJ unit of time defined in section 4.1. All simulations start with an equilibration period of 10^6 time steps, followed by a production period of 10^8 time steps.

We first calculate the cation and anion distributions along the z-axis for all considered systems; the results are summarized in Figure 5(a)–(d). In panels (a)–(b), where the dielectric contrasts are set as $\gamma_{\text{top}} = \gamma_{\text{bot}} = 0.939$, the concentrations illustrate the so-called *ion depletion effect* near the insulator-like interfaces, consistent with previous findings. Panels (c)–(d) demonstrate the complicated interplay between the dielectric confinement effect, interfacial charges, and ion valences, and their cumulative effects on the cation distribution. For all cases considered, the RBE2D results show excellent agreement with that of the HSMA and ICM-PPPM methods. The ion distribution shown in panel (c) also agrees with the result from a boundary element solver [61] and reported in [66, Figure 4(b)]. Additionally, we calculate the potential energy distribution $\mathscr{P}(U)$ for these systems and measure the discrepancy using the W_2 norm. A convergence rate of $\mathcal{O}(1/P)$ is again observed (see Figure SM2 in the supplementary material).

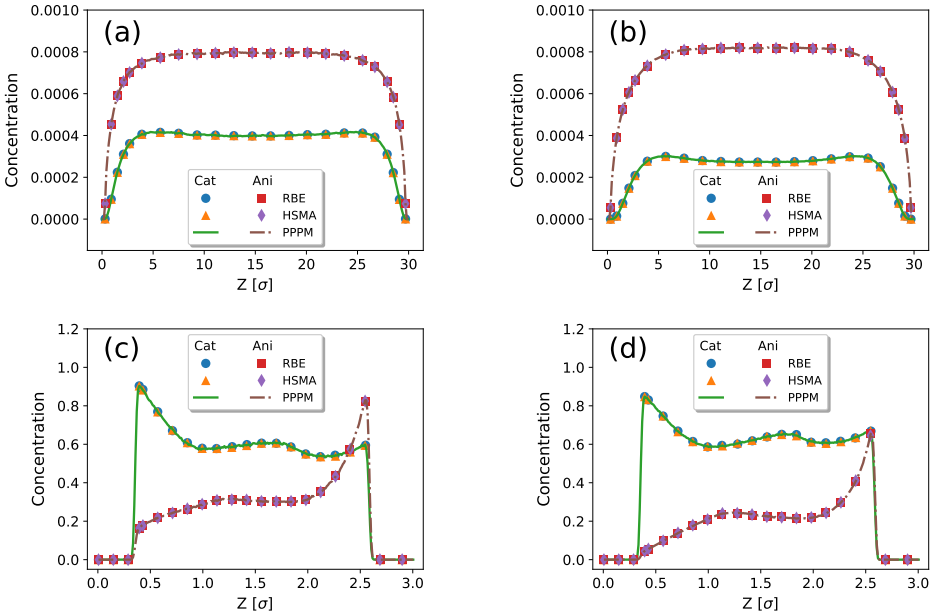

FIG. 5. *Ionic distributions for* [(a) 2 : 1 *electrolyte and* (b) 3 : 1 *electrolyte*] *between neutral interfaces with symmetric dielectric contrast, and* [(c) 2 : 1 *electrolyte and* (d) 3 : 1 *electrolyte*] *confined between walls with asymmetric dielectric contrasts and nonneutral asymmetric surface charge densities. More details about the system settings are provided in Table* SM1 *in the supplementary material. Data is shown for the RBE2D method with batch size* $P = 100$*, and the HSMA and the ICM-PPPM methods with relative error threshold* 10^{-4}.

5.2. Accuracy test case IV: Dielectrically confined SPC/E Water. We conclude the numerical tests with simulations of dielectrically confined SPC/E bulk water, and cross compare the RBE2D and ICM-PPPM methods. One can refer to section 4.2 for most of the system setups. Here the dielectric mismatches are introduced and set as $\gamma_{\text{top}} = \gamma_{\text{bot}} = -0.5$. The parameters of the ICM-PPPM method were automatically chosen [31] to achieve a relative error of $\Delta = 10^{-4}$, and the real space cutoff distance r_c was set to $12\mathring{A}$, which was selected to optimize the performance of the ICM-PPPM method.

We first examine the concentration of oxygen along the z-axis for a system comprising 53367 atoms; the results are displayed in Figure 6(a). We again find excellent agreement between the RBE2D and the ICM-PPPM when $P \geq 200$, whereas some small discrepancy is observed if one chooses $P = 100$. The MSD and VACF are also calculated and shown in Figure 6(b)–(c). The results clearly indicate that for dynamic properties of the water molecules (such as MSD and VACF), the results obtained by RBE2D are consistent with those of the ICM-PPPM across multiple time scales (fs to ns).

Finally, the CPU time and scalability data of both the RBE2D and ICM-PPPM methods are documented in Figure 6(d), based on simulating a water system containing 139968 atoms. It is observed that the RBE2D is more than 10 times faster than the ICM-PPPM method. Furthermore, the parallel efficiency is shown in the inset of Figure 6(d), which indicates that RBE2D can remain a strong scaling of 60% for up to 4000 CPU cores, while that of ICM-PPPM drops to only about 5%, again demonstrating the strong parallel efficiency of the RBE2D method. We also provide

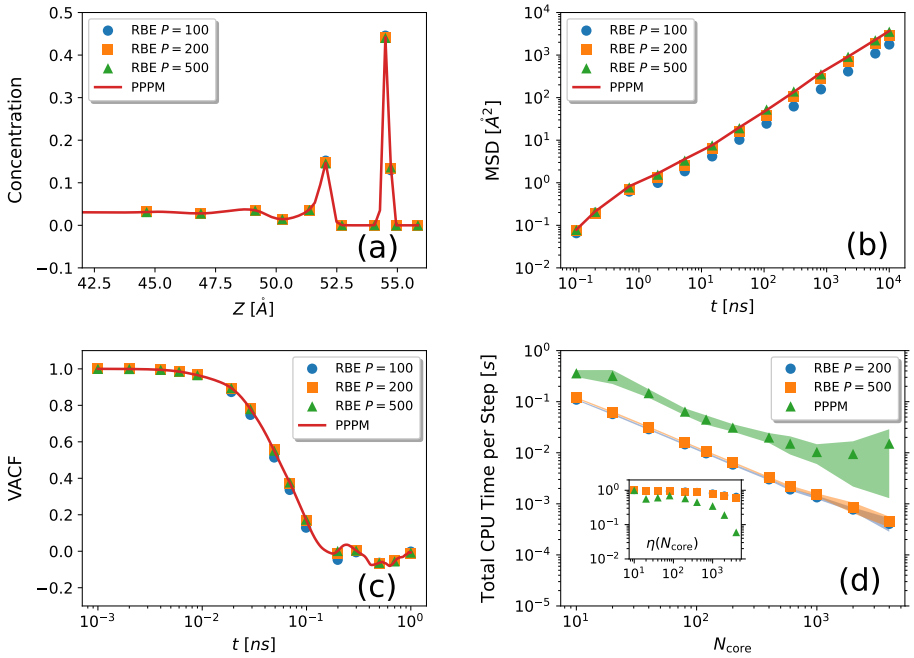

FIG. 6. *Distribution of oxygen atom s in SPC/E bulk water system* (a)*, the MSD* (b)*, the VACF* (c)*, and comparison of time performance between RBE2D (with different P) and ICM-PPPM* (d) *is studied. The inset in* (d) *shows the corresponding strong parallel efficiency $\eta(N_{core})$ defined as* (4.3)*. The results derived from the RBE2D are almost identical to those derived from the ICM-PPPM. The RBE2D based MD is about* 1.5 *orders of magnitude faster than the ICM-PPPM-based MD.*

a more detailed comparison between the RBE2D and ICM-PPPM methods in Figure SM4 in the supplementary material, using the same number of CPU cores ($N_{\text{core}} = 64$ and 1024) and a batch size of $P = 200$, with varying particle number N. The results clearly demonstrate that RBE2D outperforms ICM-PPPM across the range of N up to 10^6.

6. Conclusion. In summary, we have developed a novel RBE2D method to efficiently simulate a collection of charges in a quasi-2D geometry, with the extension to scenarios with dielectric confinement. Our method adopts an importance sampling strategy in $\boldsymbol{k}$-space and scales optimally as $\mathcal{O}(N)$ and has reduced variance. The accuracy, efficiency, and scalability of our method are demonstrated via various numerical tests. Compared to existing methods, an excellent agreement in the simulation results is observed, but with a significant reduction in the computational cost and improved strong scalability thanks to the stochastic sampling nature of our method. Thus, our method can enable highly efficient and accurate simulations for large-scale simulations of charged systems under quasi-2D confinement.

When the confined interfaces are not of planar shape, we anticipate that a boundary integral formulation can be incorporated—the polarization effect can be approximated as the field due to induced surface charges, and then in each field evaluation, RBE2D may be applied to reduce the computational cost, so that it will be capable of efficiently and accurately simulating charged particles confined by structured surfaces [61].

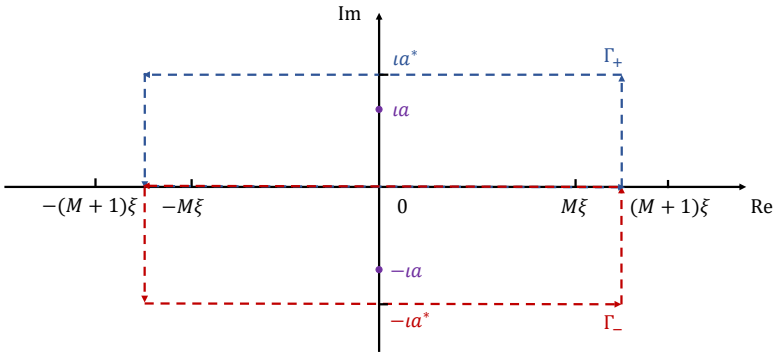

FIG. 7. *Integration contours in the error estimation of trapezoidal rule.*

We intend to compare the RBE2D method with other existing approaches in our future work. For example, our previous study [19] also focuses on quasi-2D Coulomb systems, while the RBE2D method presented here provides distinct advantages in dealing with dielectric interfaces and achieving exceptional parallel performance. Furthermore, we aim to apply the RBE2D method to other complex systems, such as membrane-protein systems and battery-electrolyte systems, where confinement effects can significantly influence their properties.

Appendix A. Quadrature error of the trapezoidal rule. We employ the method of contour integrals [11, 58] to derive a precise estimation for the error in the trapezoidal rule when discretizing (2.12) and (2.13). Consider the integral

$$I = \int_{-\infty}^{\infty} \frac{e^{-(a^2+t^2)}}{a^2+t^2} e^{\iota bt} dt, \tag{A.1}$$

where $a \geq 0$ and $b \in \mathbb{R}$. We approximate I using a $(2M+1)$-point trapezoidal rule:

$$I_{M,\xi} = \xi \sum_{j=-M}^{M} \frac{e^{-a^2-(j\xi)^2}}{a^2+(j\xi)^2} e^{\iota bj\xi}, \tag{A.2}$$

where $\xi > 0$ is the step size, and we define the remainder as $E_{M,\xi} := I - I_{M,\xi}$. Note that the integrand of I has two simple poles at $t_\pm = \pm \iota a$. Let $\Gamma_\pm$ be two positively/negatively oriented rectangular contours with vertices $(M+1/2)\xi \pm \iota a^*$, $-(M+1/2)\xi \pm \iota a^*$, $(M+1/2)\xi$, and $-(M+1/2)\xi$ (see Figure 7). We enforce $a^* > a$ so that $\Gamma_\pm$ encloses both the interval $[-M\xi, M\xi]$ and the pole $t_\pm$. By following the approach given in [11] and applying Cauchy's theorem, we can derive an estimate for $E_{M,\xi}$ in the limit $M \to \infty$:

$$E_{M,\xi} = \int_{\Gamma_+ + \Gamma_-} \frac{e^{-(a^2+t^2)+\iota bt}}{a^2+t^2} \varphi(t) dt - 2\pi\iota \mathrm{Res}\left[\frac{e^{-(a^2+t^2)+\iota bt}}{a^2+t^2} \varphi(t), \pm \iota a \right], \tag{A.3}$$

where

$$\varphi(t) = \begin{cases} \dfrac{1}{1-e^{2\pi\iota t/\xi}}, & \mathrm{Im}(t) < 0, \\ -\dfrac{1}{1-e^{-2\pi\iota t/\xi}}, & \mathrm{Im}(t) > 0, \end{cases} \tag{A.4}$$

is related to the characteristic function of the trapezoidal rule, and $\mathrm{Res}[f(t), t_0]$ denotes the residue of a function f at a pole t_0. Since the contributions from the vertical sides of $\Gamma_\pm$ vanish in the limit $M \to \infty$ and by using residue calculus, we have

$$E_{M,\xi} = \left(\int_{-\infty+\iota a^*}^{\infty+\iota a^*} - \int_{-\infty-\iota a^*}^{\infty-\iota a^*} \right) \frac{e^{-(a^2+t^2)+\iota b t}}{a^2+t^2} \varphi(t) dt + \frac{\pi}{a} \frac{e^{-ab}+e^{ab}}{1-e^{2\pi a/\xi}}. \tag{A.5}$$

In (A.5), the last term can be considered as the residue correction of the rule, while the remainder integral along $\mathrm{Im}(t) = a^*$ can be estimated as

$$\begin{aligned} \left| \int_{-\infty+\iota a^*}^{\infty+\iota a^*} \frac{e^{-(a^2+t^2)+\iota b t}}{a^2+t^2} \varphi(t) dt \right| &\le e^{(a^*)^2 - a^2 - a^* b - 2\pi a^*/\xi} \int_{-\infty}^{\infty} \frac{|a^2 + (t+\iota a^*)^2|^{-1} e^{-t^2}}{\left|1 - e^{2\pi\iota t/\xi - 2\pi a^*/\xi}\right|} dt \\ &\le \frac{\sqrt{\pi} e^{(a^*)^2 - a^2 - a^* b - 2\pi a^*/\xi}}{(a^*)^2 - a^2}. \end{aligned} \tag{A.6}$$

To obtain a closed formula, it is necessary to determine the extremum of the exponent under the condition $a^* > a > 0$. Since the range of a is not specified, we can safely choose $a^* = \pi/\xi + b/2$ if $\pi/\xi + b/2 > a$, and $a^* = \sqrt{a^2+1}$ otherwise. This choice ensures a decay rate of at least $\sim \mathcal{O}(e^{-\mathrm{sign}(\pi/\xi+b/2)|\pi/\xi+b/2|^2})$, where $\mathrm{sign}(t) = 1$ if $t > 0$, $\mathrm{sign}(t) = 0$ if $t = 0$, and $\mathrm{sign}(t) = -1$ otherwise. By following a similar procedure, we can derive that the integral along $\mathrm{Im}(t) = -a^*$ in (A.5) decays with order $\mathcal{O}(e^{-\mathrm{sign}(\pi/\xi-b/2)|\pi/\xi-b/2|^2})$. Consequently, we can conclude that

$$E_{M,\xi} = \frac{\pi}{a} \frac{e^{-ab}+e^{ab}}{1-e^{2\pi a/\xi}} + E_{\mathrm{err}}, \tag{A.7}$$

where the remainder error term can be estimated as

$$|E_{\mathrm{err}}| \sim \mathcal{O}(e^{-\mathrm{sign}(\pi/\xi-|b|/2)|\pi/\xi-|b|/2|^2}). \tag{A.8}$$

REFERENCES

[1] M. J. Abraham, T. Murtola, R. Schulz, S. Páll, J. C. Smith, B. Hess, and E. Lindahl, *GROMACS: High performance molecular simulations through multi-level parallelism from laptops to supercomputers*, SoftwareX, 1–2 (2015), pp. 19–25, https://doi.org/10.1016/j.softx.2015.06.001.

[2] A. Arnold, J. de Joannis, and C. Holm, *Electrostatics in periodic slab geometries*, I, J. Chem. Phys., 117 (2002), pp. 2496–2502, https://doi.org/10.1063/1.1491955.

[3] A. Arnold, F. Fahrenberger, C. Holm, O. Lenz, M. Bolten, H. Dachsel, R. Halver, I. Kabadshow, F. Gähler, F. Heber, et al., *Comparison of scalable fast methods for long-range interactions*, Phys. Rev. E, 88 (2013), 063308, https://doi.org/10.1103/PhysRevE.88.063308.

[4] A. Arnold and C. Holm, *MMM2D: A fast and accurate summation method for electrostatic interactions in 2D slab geometries*, Comput. Phys. Commun., 148 (2002), pp. 327–348, https://doi.org/10.1016/S0010-4655(02)00586-6.

[5] A. Ayala, S. Tomov, M. Stoyanov, and J. Dongarra, *Scalability issues in FFT computation*, in Parallel Computing Technologies, V. Malyshkin, ed., Springer, Cham, 2021, pp. 279–287.

[6] H. Berendsen, J. Grigera, and T. Straatsma, *The missing term in effective pair potentials*, J. Phys. Chem., 91 (1987), pp. 6269–6271, https://doi.org/10.1021/j100308a038.

[7] H. Cheng, L. Greengard, and V. Rokhlin, *A fast adaptive multipole algorithm in three dimensions*, J. Comput. Phys., 155 (1999), pp. 468–498, https://doi.org/10.1006/jcph.1999.6355.

[8] P. S. Crozier, R. L. Rowley, and D. Henderson, *Molecular-dynamics simulations of ion size effects on the fluid structure of aqueous electrolyte systems between charged model electrodes*, J. Chem. Phys., 114 (2001), pp. 7513–7517, https://doi.org/10.1063/1.1362290.

[9] T. Darden, D. York, and L. Pedersen, *Particle mesh Ewald: An $N \cdot \log(N)$ method for Ewald sums in large systems*, J. Chem. Phys., 98 (1993), pp. 10089–10092, https://doi.org/10.1063/1.464397.

[10] M. Deserno and C. Holm, *How to mesh up Ewald sums.* II. *An accurate error estimate for the particle-particle-particle-mesh algorithm*, J. Chem. Phys., 109 (1998), pp. 7694–7701, https://doi.org/10.1063/1.477415.

[11] J. D. Donaldson and D. Elliott, *A unified approach to quadrature rules with asymptotic estimates of their remainders*, SIAM J. Numer. Anal., 9 (1972), pp. 573–602, https://doi.org/10.1137/0709051.

[12] A. P. dos Santos, M. Girotto, and Y. Levin, *Simulations of polyelectrolyte adsorption to a dielectric like-charged surface*, J. Phys. Chem. B, 120 (2016), pp. 10387–10393, https://doi.org/10.1021/acs.jpcb.6b06002.

[13] A. P. dos Santos and Y. Levin, *Electrolytes between dielectric charged surfaces: Simulations and theory*, J. Chem. Phys., 142 (2015), 194104, https://doi.org/10.1063/1.4921221.

[14] A. Erdelyi, W. Magnus, F. Oberhettinger, and F. Tricomi, *Tables of Integral Transforms*, *Vol.* I, McGraw-Hill, 1954.

[15] U. Essmann, L. Perera, M. L. Berkowitz, T. Darden, H. Lee, and L. G. Pedersen, *A smooth particle mesh Ewald method*, J. Chem. Phys., 103 (1995), pp. 8577–8593, https://doi.org/10.1063/1.470117.

[16] P. P. Ewald, *Die Berechnung optischer und elektrostatischer Gitterpotentiale*, Ann. Phys., 369 (1921), pp. 253–287, https://doi.org/10.1002/andp.19213690304.

[17] S. E. Feller, Y. Zhang, R. W. Pastor, and B. R. Brooks, *Constant pressure molecular dynamics simulation: The Langevin piston method*, J. Chem. Phys., 103 (1995), pp. 4613–4621, https://doi.org/10.1063/1.470648.

[18] D. Frenkel and B. Smit, *Understanding Molecular Simulation: From Algorithms to Applications*, Elsevier, 2023.

[19] Z. Gan, X. Gao, J. Liang, and Z. Xu, *Fast algorithm for quasi-2D Coulomb systems*, J. Comput. Phys., 524 (2025), 113733, https://doi.org/10.1016/j.jcp.2025.113733.

[20] L. Greengard and V. Rokhlin, *A fast algorithm for particle simulations*, J. Comput. Phys., 73 (1987), pp. 325–348, https://doi.org/10.1016/0021-9991(87)90140-9.

[21] A. Grzybowski, E. Gwóźdź, and A. Bródka, *Ewald summation of electrostatic interactions in molecular dynamics of a three-dimensional system with periodicity in two directions*, Phys. Rev. B, 61 (2000), pp. 6706–6712, https://doi.org/10.1103/PhysRevB.61.6706.

[22] R. W. Hockney and J. W. Eastwood, *Computer Simulation Using Particles*, CRC Press, 2021.

[23] W. G. Hoover, *Canonical dynamics: Equilibrium phase-space distributions*, Phys. Rev. A, 31 (1985), pp. 1695–1697, https://doi.org/10.1103/PhysRevA.31.1695.

[24] Z. Hu, *Infinite boundary terms of Ewald sums and pairwise interactions for electrostatics in bulk and at interfaces*, J. Chem. Theory Comput., 10 (2014), pp. 5254–5264, https://doi.org/10.1021/ct500704m.

[25] J. D. Jackson, *Classical Electrodynamics*, 3rd ed., Wiley, New York, 1999.

[26] S. Jin, L. Li, and J.-G. Liu, *Random Batch Methods (RBM) for interacting particle systems*, J. Comput. Phys., 400 (2020), 108877, https://doi.org/10.1016/j.jcp.2019.108877.

[27] S. Jin, L. Li, and J.-G. Liu, *Convergence of the random batch method for interacting particles with disparate species and weights*, SIAM J. Numer. Anal., 59 (2021), pp. 746–768, https://doi.org/10.1137/20M1327641.

[28] S. Jin, L. Li, and Y. Sun, *On the random batch method for second order interacting particle systems*, Multiscale Model. Simul., 20 (2022), pp. 741–768, https://doi.org/10.1137/20M1383069.

[29] S. Jin, L. Li, Z. Xu, and Y. Zhao, *A random batch Ewald method for particle systems with Coulomb interactions*, SIAM J. Sci. Comput., 43 (2021), pp. B937–B960, https://doi.org/10.1137/20M1371385.

[30] J. Kim, Z. Ou, M. R. Jones, X. Song, and Q. Chen, *Imaging the polymerization of multivalent nanoparticles in solution*, Nat. Commun., 8 (2017), 761, https://doi.org/10.1038/s41467-017-00857-1.

[31] J. Kolafa and J. W. Perram, *Cutoff errors in the Ewald summation formulae for point charge systems*, Mol. Simul., 9 (1992), pp. 351–368, https://doi.org/10.1080/08927029208049126.

[32] N. Kolbe, *nklb/wasserstein-distance: v*1.0, Apr. 2024, https://doi.org/10.5281/zenodo.10912241.

[33] A. Kumar and P. Ahluwalia, *Tunable dielectric response of transition metals dichalcogenides MX_2 ($M = Mo, W$; $X = S, Se, Te$): Effect of quantum confinement*, Phys. B, 407 (2012), pp. 4627–4634, https://doi.org/10.1016/j.physb.2012.08.034.

[34] Y. Levin, *Electrostatic correlations: From plasma to biology*, Rep. Prog. Phys., 65 (2002), pp. 1577–1632, https://doi.org/10.1088/0034-4885/65/11/201.

[35] J. Liang, P. Tan, L. Hong, S. Jin, Z. Xu, and L. Li, *A random batch Ewald method for charged particles in the isothermal–isobaric ensemble*, J. Chem. Phys., 157 (2022), 144102, https://doi.org/10.1063/5.0107140.

[36] J. Liang, P. Tan, Y. Zhao, L. Li, S. Jin, L. Hong, and Z. Xu, *Superscalability of the random batch Ewald method*, J. Chem. Phys., 156 (2022), 014114, https://doi.org/10.1063/5.0073424.

[37] J. Liang, Z. Xu, and Y. Zhao, *Energy stable scheme for random batch molecular dynamics*, J. Chem. Phys., 160 (2024), 034101, https://doi.org/10.1063/5.0187108.

[38] J. Liang, Z. Xu, and Q. Zhou, *Random batch sum-of-Gaussians method for molecular dynamics simulations of particle systems*, SIAM J. Sci. Comput., 45 (2023), pp. B591–B617, https://doi.org/10.1137/22M1497201.

[39] J. Liang, J. Yuan, E. Luijten, and Z. Xu, *Harmonic surface mapping algorithm for molecular dynamics simulations of particle systems with planar dielectric interfaces*, J. Chem. Phys., 152 (2020), 134109, https://doi.org/10.1063/5.0003293.

[40] J. Liang, J. Yuan, and Z. Xu, *HSMA: An $O(N)$ electrostatics package implemented in LAMMPS*, Comput. Phys. Commun., 276 (2022), 108332, https://doi.org/10.1016/j.cpc.2022.108332.

[41] D. Lindbo and A.-K. Tornberg, *Fast and spectrally accurate Ewald summation for 2-periodic electrostatic systems*, J. Chem. Phys., 136 (2012), 164111, https://doi.org/10.1063/1.4704177.

[42] M. Ma, Z. Xu, and L. Zhang, *Modified Poisson–Nernst–Planck model with Coulomb and hard-sphere correlations*, SIAM J. Appl. Math., 81 (2021), pp. 1645–1667, https://doi.org/10.1137/19M1310098.

[43] K. Mangold, P. Leiderer, and C. Bechinger, *Phase transitions of colloidal monolayers in periodic pinning arrays*, Phys. Rev. Lett., 90 (2003), 158302, https://doi.org/10.1103/PhysRevLett.90.158302.

[44] O. Maxian, R. P. Peláez, L. Greengard, and A. Donev, *A fast spectral method for electrostatics in doubly periodic slit channels*, J. Chem. Phys., 154 (2021), 204107, https://doi.org/10.1063/5.0044677.

[45] M. Mazars, *Long ranged interactions in computer simulations and for quasi-2D systems*, Phys. Rep., 500 (2011), pp. 43–116, https://doi.org/10.1016/j.physrep.2010.11.004.

[46] N. Metropolis, A. W. Rosenbluth, M. N. Rosenbluth, A. H. Teller, and E. Teller, *Equation of state calculations by fast computing machines*, J. Chem. Phys., 21 (1953), pp. 1087–1092, https://doi.org/10.1063/1.1699114.

[47] T. D. Nguyen, H. Li, D. Bagchi, F. J. Solis, and M. O. de la Cruz, *Incorporating surface polarization effects into large-scale coarse-grained molecular dynamics simulation*, Comput. Phys. Commun., 241 (2019), pp. 80–91, https://doi.org/10.1016/j.cpc.2019.03.006.

[48] K. S. Novoselov, A. K. Geim, S. V. Morozov, D. Jiang, Y. Zhang, S. V. Dubonos, I. V. Grigorieva, and A. A. Firsov, *Electric field effect in atomically thin carbon films*, Science, 306 (2004), pp. 666–669, https://doi.org/10.1126/science.1102896.

[49] C. Pan and Z. Hu, *Rigorous error bounds for Ewald summation of electrostatics at planar interfaces*, J. Chem. Theory Comput., 10 (2014), pp. 534–542, https://doi.org/10.1021/ct400839x.

[50] D. Parry, *The electrostatic potential in the surface region of an ionic crystal*, Surf. Sci., 49 (1975), pp. 433–440, https://doi.org/10.1016/0039-6028(75)90362-3.

[51] R. Pei, T. Askham, L. Greengard, and S. Jiang, *A fast method for imposing periodic boundary conditions on arbitrarily-shaped lattices in two dimensions*, J. Comput. Phys., 474 (2023), 111792, https://doi.org/10.1016/j.jcp.2022.111792.

[52] U. Raviv, P. Laurat, and J. Klein, *Fluidity of water confined to subnanometre films*, Nature, 413 (2001), pp. 51–54, https://doi.org/10.1038/35092523.

[53] F. Santambrogio, *Optimal Transport for Applied Mathematicians*, Progr. Nonlinear Diff. Equations Appl. 87, Birkhäuser, Cham, 2015, https://doi.org/10.1007/978-3-319-20828-2.

[54] E. R. Smith, *Electrostatic energy in ionic crystals*, Proc. R. Soc. London A Math. Phys. Sci., 375 (1981), pp. 475–505, https://doi.org/10.1098/rspa.1981.0064.

[55] E. Spohr, *Effect of electrostatic boundary conditions and system size on the interfacial properties of water and aqueous solutions*, J. Chem. Phys., 107 (1997), pp. 6342–6348, https://doi.org/10.1063/1.474295.

[56] A. P. Thompson, H. M. Aktulga, R. Berger, D. S. Bolintineanu, W. M. Brown, P. S. Crozier, P. J. in't Veld, A. Kohlmeyer, S. G. Moore, T. D. Nguyen, et al., *LAMMPS—a flexible simulation tool for particle-based materials modeling at the atomic, meso, and continuum scales*, Comput. Phys. Commun., 271 (2021), 108171, https://doi.org/10.1016/j.cpc.2021.108171.

[57] A.-K. Tornberg, *The Ewald sums for singly, doubly and triply periodic electrostatic systems*, Adv. Comput. Math., 42 (2016), pp. 227–248, https://doi.org/10.1007/s10444-015-9422-3.

[58] L. N. Trefethen and J. A. C. Weideman, *The exponentially convergent trapezoidal rule*, SIAM Rev., 56 (2014), pp. 385–458, https://doi.org/10.1137/130932132.

[59] S. Tyagi, A. Arnold, and C. Holm, *ICMMM2D: An accurate method to include planar dielectric interfaces via image charge summation*, J. Chem. Phys., 127 (2007), 154723, https://doi.org/10.1063/1.2790428.

[60] S. Tyagi, A. Arnold, and C. Holm, *Electrostatic layer correction with image charges: A linear scaling method to treat slab 2D+h systems with dielectric interfaces*, J. Chem. Phys., 129 (2008), 204102, https://doi.org/10.1063/1.3021064.

[61] H. Wu, H. Li, F. J. Solis, M. Olvera de la Cruz, and E. Luijten, *Asymmetric electrolytes near structured dielectric interfaces*, J. Chem. Phys., 149 (2018), 164701, https://doi.org/10.1063/1.5047550.

[62] W. Yan and M. Shelley, *Flexibly imposing periodicity in kernel independent FMM: A multipole-to-local operator approach*, J. Comput. Phys., 355 (2018), pp. 214–232, https://doi.org/10.1016/j.jcp.2017.11.012.

[63] I.-C. Yeh and M. L. Berkowitz, *Ewald summation for systems with slab geometry*, J. Chem. Phys., 111 (1999), pp. 3155–3162, https://doi.org/10.1063/1.479595.

[64] S. Yi, C. Pan, and Z. Hu, *Note: A pairwise form of the Ewald sum for non-neutral systems*, J. Chem. Phys., 147 (2017), 126101, https://doi.org/10.1063/1.4998320.

[65] L. Ying, G. Biros, and D. Zorin, *A kernel-independent adaptive fast multipole algorithm in two and three dimensions*, J. Comput. Phys., 196 (2004), pp. 591–626, https://doi.org/10.1016/j.jcp.2003.11.021.

[66] J. Yuan, H. S. Antila, and E. Luijten, *Particle–particle particle–mesh algorithm for electrolytes between charged dielectric interfaces*, J. Chem. Phys., 154 (2021), 094115, https://doi.org/10.1063/5.0035944.

[67] Z. Zhu, D. Wang, Y. Tian, and L. Jiang, *Ion/molecule transportation in nanopores and nanochannels: From critical principles to diverse functions*, J. Amer. Chem. Soc., 141 (2019), pp. 8658–8669, https://doi.org/10.1021/jacs.9b00086.